



NAVAL POSTGRADUATE SCHOOL

MONTEREY, CALIFORNIA

THESIS

**PROCESSING-MICROSTRUCTURE-PROPERTY
RELATIONSHIPS FOR COLD SPRAY POWDER
DEPOSITION OF Al-Cu ALLOYS**

by

Jeremy D. Leazer

June 2015

Thesis Advisor:
Co-Advisor:

Sarath K. Menon
Luke N. Brewer

Approved for public release; distribution is unlimited

THIS PAGE INTENTIONALLY LEFT BLANK

| | | | | |
|---|---|--|--|--|
| REPORT DOCUMENTATION PAGE | | | <i>Form Approved OMB No. 0704-0188</i> | |
| Public reporting burden for this collection of information is estimated to average 1 hour per response, including the time for reviewing instruction, searching existing data sources, gathering and maintaining the data needed, and completing and reviewing the collection of information. Send comments regarding this burden estimate or any other aspect of this collection of information, including suggestions for reducing this burden, to Washington headquarters Services, Directorate for Information Operations and Reports, 1215 Jefferson Davis Highway, Suite 1204, Arlington, VA 22202-4302, and to the Office of Management and Budget, Paperwork Reduction Project (0704-0188) Washington, DC 20503. | | | | |
| 1. AGENCY USE ONLY (Leave blank) | | 2. REPORT DATE June 2015 | 3. REPORT TYPE AND DATES COVERED Master's Thesis | |
| 4. TITLE AND SUBTITLE PROCESSING-MICROSTRUCTURE-PROPERTY RELATIONSHIPS FOR COLD SPRAY POWDER DEPOSITION OF Al-Cu ALLOYS | | | 5. FUNDING NUMBERS | |
| 6. AUTHOR(S) Jeremy D. Leazer | | | | |
| 7. PERFORMING ORGANIZATION NAME(S) AND ADDRESS(ES) Naval Postgraduate School Monterey, CA 93943-5000 | | | 8. PERFORMING ORGANIZATION REPORT NUMBER | |
| 9. SPONSORING /MONITORING AGENCY NAME(S) AND ADDRESS(ES) N/A | | | 10. SPONSORING/MONITORING AGENCY REPORT NUMBER | |
| 11. SUPPLEMENTARY NOTES The views expressed in this thesis are those of the author and do not reflect the official policy or position of the Department of Defense or the U.S. Government. IRB Protocol number ____ N/A ____. | | | | |
| 12a. DISTRIBUTION / AVAILABILITY STATEMENT Approved for public release; distribution is unlimited | | | 12b. DISTRIBUTION CODE A | |
| 13. ABSTRACT (maximum 200 words) This thesis presents research on the cold gas-dynamic spray process applied to the deposition of aluminum-copper alloy coatings. Cold spray deposition is a process utilized to create corrosion protection coatings and to perform additive repair for aluminum structures. This thesis utilized a series of Al-Cu binary alloy powders, from 2–5 weight percent copper and characterized their chemistry and microstructure. The powders were deposited using the cold spray approach to study the systematic increase of the alloying agent on the deposition process and coating characteristics. Deposition efficiency, critical velocity, coating thickness, hardness, porosity, and microstructure were all characterized as functions of carrier gas pressure, carrier gas temperature and feedstock powder copper composition. This thesis has demonstrated that all of the aluminum copper powders utilized can be successfully deposited via the low-pressure cold spray process with helium as the carrier gas. The copper content of the powders has a direct effect on the volume fraction of Al ₂ Cu intermetallics, and on the coating hardness, while having no measurable effect on critical velocity for deposition or the coating thickness per pass. | | | | |
| 14. SUBJECT TERMS cold spray, aluminum copper, particle velocity, critical velocity | | | 15. NUMBER OF PAGES 99 | |
| | | | 16. PRICE CODE | |
| 17. SECURITY CLASSIFICATION OF REPORT Unclassified | 18. SECURITY CLASSIFICATION OF THIS PAGE Unclassified | 19. SECURITY CLASSIFICATION OF ABSTRACT Unclassified | 20. LIMITATION OF ABSTRACT UU | |

THIS PAGE INTENTIONALLY LEFT BLANK

Approved for public release; distribution is unlimited

**PROCESSING-MICROSTRUCTURE-PROPERTY RELATIONSHIPS FOR
COLD SPRAY POWDER DEPOSITION OF Al-Cu ALLOYS**

Jeremy D. Leazer
Lieutenant, United States Navy
B.E., State University of New York Maritime College, 2008

Submitted in partial fulfillment of the
requirements for the degree of

MASTER OF SCIENCE IN MECHANICAL ENGINEERING

from the

**NAVAL POSTGRADUATE SCHOOL
June 2015**

Author: Jeremy D. Leazer

Approved by: Sarath K. Menon
Thesis Advisor

Luke N. Brewer
Co-Advisor

Garth V. Hobson
Chair, Department of Mechanical and Aerospace Engineering

THIS PAGE INTENTIONALLY LEFT BLANK

ABSTRACT

This thesis presents research on the cold gas-dynamic spray process applied to the deposition of aluminum-copper alloy coatings. Cold spray deposition is a process utilized to create corrosion protection coatings and to perform additive repair for aluminum structures. This thesis utilized a series of Al-Cu binary alloy powders, from 2–5 weight percent copper and characterized their chemistry and microstructure. The powders were deposited using the cold spray approach to study the systematic increase of the alloying agent on the deposition process and coating characteristics. Deposition efficiency, critical velocity, coating thickness, hardness, porosity, and microstructure were all characterized as functions of carrier gas pressure, carrier gas temperature and feedstock powder copper composition. This thesis has demonstrated that all of the aluminum copper powders utilized can be successfully deposited via the low-pressure cold spray process with helium as the carrier gas. The copper content of the powders has a direct effect on the volume fraction of Al_2Cu intermetallics, and on the coating hardness, while having no measurable effect on critical velocity for deposition or the coating thickness per pass.

THIS PAGE INTENTIONALLY LEFT BLANK

TABLE OF CONTENTS

| | | |
|------------------|---|-----------|
| I. | INTRODUCTION..... | 1 |
| A. | MOTIVATION | 1 |
| B. | LITERATURE REVIEW | 3 |
| 1. | Cold Spray Deposition Process and Characteristics..... | 3 |
| 2. | Utilizing Aluminum Alloy Powder in the Cold Spray Deposition Process | 12 |
| C. | OBJECTIVES | 14 |
| II. | EXPERIMENTAL METHODS | 17 |
| A. | POWDER PRODUCTION | 17 |
| B. | POWDER CHARACTERIZATION | 18 |
| C. | COATING PRODUCTION | 19 |
| 1. | Cold Spray Deposition Experiments | 19 |
| 2. | Particle Velocity Experiments | 21 |
| 3. | One-Dimensional MATLAB Simulation of Centerline SST Model Series C UltiLife Nozzle | 24 |
| 4. | Hardness | 24 |
| III. | RESULTS | 25 |
| A. | POWDER CHARACTERISTICS..... | 25 |
| 1. | Particle Sizing..... | 25 |
| 2. | Particle Morphology | 26 |
| 3. | EDS Quantification | 31 |
| 4. | X-ray Maps | 34 |
| 5. | X-ray Diffraction..... | 37 |
| B. | COLD SPRAY COATING CHARACTERISTICS..... | 40 |
| 1. | Cold Spray Deposition Experiments | 40 |
| 2. | Critical Velocity Experiments..... | 44 |
| 3. | MATLAB Simulation of Centerline SST UltiLife Nozzle | 47 |
| 4. | Coating Microstructures | 49 |
| 5. | Hardness | 54 |
| IV. | DISCUSSION | 57 |
| A. | THE ROLE OF COPPER..... | 57 |
| B. | CALCULATION OF CRITICAL VELOCITY..... | 59 |
| C. | HOW FAR THE AS-RECEIVED POWDERS ARE FROM EQUILIBRIUM | 62 |
| D. | RELATIONSHIP OF POWDER FLOWRATE, COATING THICKNESS, AND DEPOSITION EFFICIENCY..... | 64 |
| V. | CONCLUSION | 67 |
| APPENDIX. | ONE-DIMENSIONAL MODEL SIMULATION MATLAB CODE | 69 |
| A. | HELIUM..... | 69 |
| B. | CREATFIGURE CODE | 75 |

| | |
|--|-----------|
| LIST OF REFERENCES | 77 |
| INITIAL DISTRIBUTION LIST | 81 |

LIST OF FIGURES

| | | |
|------------|--|----|
| Figure 1. | Cold spray of aluminum/aluminum oxide to repair 7075-T6 snap ring groove. A) Damaged area, B) Areas requiring repair, and C) Cold-sprayed aluminum machined to original dimensions, after [3]. | 2 |
| Figure 2. | Gas temperature versus particle velocity for the different thermal spray methods, from [6]. | 4 |
| Figure 3. | Diagram showing the low-pressure cold spray process, from [2]. | 4 |
| Figure 4. | MATLAB simulation of: A) Particle velocity at nozzle exit as a function of carrier gas inlet temperature and pressure, and B) Particle velocity vs position in nozzle, at 1.21 MPa (175 psi), due to a change in carrier gas temperature, after [12]. | 6 |
| Figure 5. | Particle velocity distributions for copper sprayed onto aluminum, from [17]. | 7 |
| Figure 6. | MATLAB simulation utilizing the one-dimensional fluid dynamics equations for A) particle velocity at the nozzle exit as a function of temperature and pressure, and B) particle velocity versus position in the nozzle, at 275°C, at a given pressure, after [12]. | 9 |
| Figure 7. | 1-D and CFD calculated results of accelerating aluminum particles with nitrogen, from [13]. | 11 |
| Figure 8. | Centerline SST Model Series C low-pressure cold spray system installed at the Naval Postgraduate School. | 20 |
| Figure 9. | Tecnar setup for the particle velocity experiment showing A) rear view, and B) side view. Image from [12]. | 22 |
| Figure 10. | Critical velocity as it is calculated using DE. | 23 |
| Figure 11. | Particle sized distributions for the Al-Cu powders received from Valimet, Inc. | 25 |
| Figure 12. | Secondary electron images of the Al-Cu powders as received. | 27 |
| Figure 13. | ILSE and BSE images of the as-received powders at 2000x magnification. | 28 |
| Figure 14. | Backscatter images of the as-received powders. The cellular structure is similar for all of the powders except the Al-2Cu wt%. | 29 |
| Figure 15. | Average cellular spacing of the as-received powders with cross sections between 15–30 μm . | 30 |
| Figure 16. | Graph representing the frequency of the measured cellular spacing for the as-received powders. | 30 |
| Figure 17. | EDS point spectra for Al-5Cu powder. | 32 |
| Figure 18. | EDS quantification of Al-5Cu powder. | 33 |
| Figure 19. | Average EDS values for the powders. Points 1 and 3 correspond to the center of cells while point 2 is the Cu rich boundary. | 34 |
| Figure 20. | EDX maps showing the components (Al and Cu) of Al-2Cu. | 35 |
| Figure 21. | EDX maps showing the components (Al and Cu) of Al-3Cu. | 35 |
| Figure 22. | EDX maps showing the components (Al and Cu) of Al-4Cu. | 36 |
| Figure 23. | EDX maps showing the components (Al and Cu) of Al-5Cu. | 36 |
| Figure 24. | X-ray diffraction pattern for Al-5Cu powder as received. | 37 |

| | | |
|------------|--|----|
| Figure 25. | X-ray diffraction pattern of the four as-received powders. The unknown peak is a possible contaminant in the sample. | 38 |
| Figure 26. | X-ray diffraction patterns comparing the as-received powders and the annealed powders for A) Al-2Cu and B) Al-5Cu, after [12]. | 39 |
| Figure 27. | Wt% of Al ₂ Cu as determined by Rietveld analysis and the lever rule. | 40 |
| Figure 28. | Deposition results for the carrier gas temperature of 275°C and pressure 1.21 MPa (175 psi). | 43 |
| Figure 29. | Deposition efficiency of the various temperature and pressure combinations for each of the powders. | 43 |
| Figure 30. | Measured particle velocities and calculated critical velocities for A) Al-2Cu at 225°C and 1.21 MPa (175 psi), B) Al-5Cu at 275°C and 1.21 MPa (175 psi), C) Al-2Cu at 275°C and 1.55 MPa (225 psi), and D) Al-5Cu at 325°C and 1.21 MPa (175 psi). | 45 |
| Figure 31. | Measured particle velocity distributions of A) Al-2Cu at 0.97 MPa (140 psi), B) Al-5Cu at 1.21 MPa (175 psi), C) Al-2Cu at 225°C, and D) Al-5Cu at 275°C. | 46 |
| Figure 32. | Velocity profile of Al-2Cu and Al-5Cu at 275°C and 1.21 MPa (175 psi). | 47 |
| Figure 33. | Comparison of measured and simulated particle velocities at 275°C and 1.21 MPa (175 psi) for A) Al-2Cu and B) Al-5Cu. Simulated data after [12]. | 48 |
| Figure 34. | BSE micrographs, at 100x magnification, of cold-sprayed coating/substrate interface with helium gas at 275°C and 1.21 MPa (175 psi). | 50 |
| Figure 35. | BSE micrographs, at 500x magnification, of cold-sprayed coating/substrate interface with helium gas at 275°C and 1.21 MPa (175 psi). | 51 |
| Figure 36. | BSE micrographs, at 1000x magnification, of cold-sprayed coating/substrate interface with helium gas at 275°C and 1.21 MPa (175 psi). | 52 |
| Figure 37. | BSE micrographs, at 2000x magnification, of the center of the cold-sprayed coatings with helium gas at 275°C and 1.21 MPa (175 psi). | 53 |
| Figure 38. | ILSE micrograph showing crack formation in cold spray deposition as depicted by the red arrows in A) Al-3Cu cold spray coating along the substrate interface and B) Al-5Cu cold spray coating. | 53 |
| Figure 39. | Hardness of the cold spray deposits as a function of wt% copper. | 54 |
| Figure 40. | Critical velocity as determined by Equation 3 [19]. The Tabor approximation utilized the work of H. K. Hardy [40] to estimate the flow strength. | 61 |
| Figure 41. | Binary phase diagram of the Al-Cu system showing the variation in solutionizing temperatures up to 6 wt% Cu, after [43]. | 63 |

LIST OF TABLES

| | | |
|-----------|---|----|
| Table 1. | Light element analysis of the Al-Cu binary powders produced from gas atomization with nitrogen gas. | 17 |
| Table 2. | Conditions used in the cold spray deposition experiments. | 21 |
| Table 3. | Combination of the pressures and temperatures used for velocity and deposition sprays. All other conditions were held the same. | 23 |
| Table 4. | Al-Cu particle size characteristics. | 26 |
| Table 5. | Cellular spacing characteristics of the as-received powders. | 31 |
| Table 6. | Wt% Al and Cu from EDS K α measurements for Al-5Cu powder. | 33 |
| Table 7. | Summary of the spray conditions used for deposition experiments. | 42 |
| Table 8. | Summary of cold spray parameters, thickness, and deposition efficiency for the cold spray experiments of Al-2Cu performed with compressed air. | 44 |
| Table 9. | Summary of critical velocity, deposition efficiency, calculated average particle velocity, and calculated average particle velocity. | 46 |
| Table 10. | Vickers hardness results of all four powders sprayed at various temperatures and pressures. | 55 |
| Table 11. | Parameters used to calculate critical velocity from equation 5. | 60 |
| Table 12. | Weight percent of Al ₂ Cu as a result of x-ray diffraction for the as-received and annealed powders and from lever rule calculations. | 64 |

THIS PAGE INTENTIONALLY LEFT BLANK

LIST OF ACRONYMS AND ABBREVIATIONS

| | |
|----------------|--------------------------------------|
| AA | aluminum alloy |
| Al | aluminum |
| Al-Cu | aluminum-copper |
| BSE | backscatter electron |
| CP | commercially pure |
| Cu | copper |
| DE | deposition efficiency |
| EDS | energy dispersive spectroscopy |
| EDX | energy dispersive x-ray spectroscopy |
| He | helium |
| HP | high purity |
| Hv | hardness value |
| ILSE | in-lens secondary electron |
| Mg | magnesium |
| N ₂ | nitrogen |
| SEM | scanning electron microscope |
| wt% | weight percent |
| XRD | x-ray diffraction |

THIS PAGE INTENTIONALLY LEFT BLANK

ACKNOWLEDGMENTS

I would like to first thank Dr. Luke Brewer for all of his guidance in completing my research. Your infectious attitude toward engineering materials and dedication to students is greatly missed at NPS. I have benefitted professionally and personally from the time we have spent together in the classroom and laboratory.

I would also like to thank Dr. Sarath Menon for all of his support. The close proximity of your office to labs was crucial, as you were always nearby to answer my many questions. The expertise you shared in metallography and characterization was an essential resource for the completion of my research.

I am grateful for the work of Jennifer Wolk and Ben Bouffard, both of Naval Surface Warfare Center, Carderock Division; and Fred Lancaster and Joseph Christophersen, both of NAVAIR, for their hard work in support of the project and my research. I would not have been able to accomplish all that I did without your support. Not only did you put in countless hours performing experiments, you also took the time to get me up to speed so I could be a contributing member of the team.

I am grateful for the funding support from Mr. William Nickerson of the Office of Naval Research (Code 35 Sea-Based Aviation Structures and Materials). Without his support, none of this research would be accomplished.

Last, but certainly not least, I would like to thank my family. My children, Layla, Keira, and Logan, are always there to lift my spirits no matter how long my day has been. I cannot begin to thank my wife, Michele, enough. You have been a constant source of support and have selflessly taken care of our home and children. All that I have accomplished is because of you. I love you all so much.

THIS PAGE INTENTIONALLY LEFT BLANK

I. INTRODUCTION

A. MOTIVATION

Since the first flight by the Wright brothers in 1903, the design of aircraft and their components has made them more aerodynamic, faster, and more durable. Despite all of the design and technology advancements, however, there are two problems that cannot be eliminated: corrosion and mechanical failure. Considerable time and money have been spent in an effort to prevent corrosion and mechanical failure [1]. There are many techniques to prevent or minimize corrosion, such as material selection, cathodic protection, and the application of paint or other coatings. Material selection, design, and processing are methods used to minimize mechanical failure. Despite all of the efforts put toward preventing failure, failure will still occur, and repair techniques will be needed to return a component to operation. In particular, repair methods that allow restoration of the component in place will greatly reduce labor costs and lost assets in an operational environment. Thermal spray, specifically cold gas dynamic spray, or “cold spray” as it more commonly known, is a method of repair that can be used for in-place component restoration. Cold spray deposition adds solid-state material to a component with similar mechanical properties, which is ideal when a coating is applied to prevent corrosion or restore material tolerances. Low-pressure (≤ 2 MPa [300 psi]) cold spray has been effective in the dimensional restoration of Al and Mg alloy aircraft components made from 6061, 7075 and other more exotic alloys [2]. After the buildup material from cold spray, repaired areas were machined and finished using standard shop methods to return them to service while meeting all requirements of the Federal Aviation Administration (FAA) [2]. Using existing gas and air systems in repair shops or onboard ships, cold spray units can be rapidly put into place to allow for similar on-site repairs of many structures and vessels.

There has been success in spraying pure aluminum (Al) and aluminum alloys (AA) for dimensional restoration of structural components, but it has not yet been shown that cold spray deposition can be used for load-bearing components. The use of cold spray to deposit commercially pure (CP) aluminum, aluminum/aluminum oxide mixture,

and aluminum/aluminum oxide/zinc mixture for the repair of the U.S. Army's 7075-T6 aluminum mast support system proved successful. The panels coated with CP-aluminum were subjected to a neutral salt spray testing and showed no signs of corrosion after 7000 hours [3]. The machinability and structural integrity of the cold-sprayed components were determined to be acceptable and demonstrated that the method is capable of repairing damage from corrosion and mechanical wear, as shown in Figure 1 [3]. Cold spray proved to be a cost effective and viable repair option for otherwise unserviceable components that are critical for the safe operation of the helicopter.



Figure 1. Cold spray of aluminum/aluminum oxide to repair 7075-T6 snap ring groove. A) Damaged area, B) Areas requiring repair, and C) Cold-sprayed aluminum machined to original dimensions, after [3].

Cold spray deposition can also be used as an effective corrosion protection coating. Commercially pure Al (99.5 weight percent [wt%]), high purity (HP) Al (99.95 wt%), AA5536 (Al-5% wt% Mg), and AA4047 (Al-12 wt% Si) were cold sprayed on Al-Mg alloys in an attempt to produce a corrosion and mechanical impact barrier with high hardness and coating adhesion while protecting against galvanic and crevice corrosion [4]. The mechanical properties (thickness, hardness, bond strength, and visual appearance of the cross section) and corrosion resistance of each powder coating were then assessed. The corrosion resistance of each coating was evaluated by accelerated salt spray, open circuit galvanic coupling, and crevice corrosion testing, with the HP aluminum proving the most resistant to galvanic corrosion [5]. All of the coatings exhibited dense cross sections, bonding strength in excess of MIL-STD-2138A (Metal-Sprayed Coatings for Corrosion Protection Aboard Naval Ships), and hardness values exceeding 40 Hv with AA5536 having the highest hardness (124 Hv) [5]. The cold spray process was utilized to

apply a corrosion barrier coating that has desirable hardness and galvanic compatibility when applied to Mg alloys.

B. LITERATURE REVIEW

1. Cold Spray Deposition Process and Characteristics

Cold spray is one many types of thermal spray processes, such as plasma spray, flame spray, and high velocity oxygen fuel spraying. These methods apply a metallic coating or add material to restore corroded or damaged material. Thermal spray techniques share many advantages, such as thick coatings at high deposition rates, a wide variety of materials available for deposit, and an even greater range of materials for use as substrates [6]. Thermal spraying, however, is not without limitations; the coatings produced can exhibit high porosity and form oxides [6]. A major difference between the other thermal spray methods and cold spray is that the other methods heat the powder to above its melting point, which can significantly change the material's microstructure and mechanical properties [6]. The sprayed powder's high temperature can also heat the substrate, possibly resulting in a shift of properties. As seen in Figure 2, cold spray is conducted at lower temperatures and higher particle velocities than other thermal spray techniques. The higher velocity allows for a denser deposition, and therefore less porosity. The higher density is due to the lack of splashing common in thermal spray, as cold spray deposits solid-state material that has a peening effect caused by incoming high velocity particles deforming the underlying, previously deposited particles, closing any small gaps or pores [6]. Cold spray has the advantages of low thermal impact to the substrate, no combustion fuels/gases, no melting of the coating material, and a resultant coating with high density. The cold spray process also allows coatings to be applied in any location the portable unit can reach.

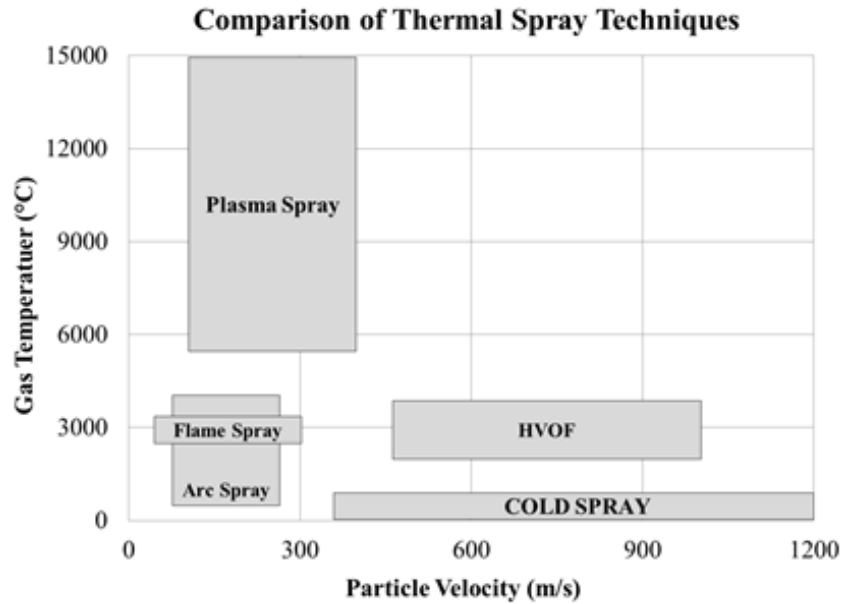


Figure 2. Gas temperature versus particle velocity for the different thermal spray methods, from [6].¹

Cold spray is a solid-state material deposition process that bonds powder particles with a substrate using the kinetic energy of the particles [7]. A carrier gas (He, N₂, Air) is used to accelerate the powder particles to high velocities, between 500–1200 m/s, that impact and bond with the substrate through plastic deformation [7]–[10]. A diagram of the low-pressure cold spray process is shown in Figure 3.

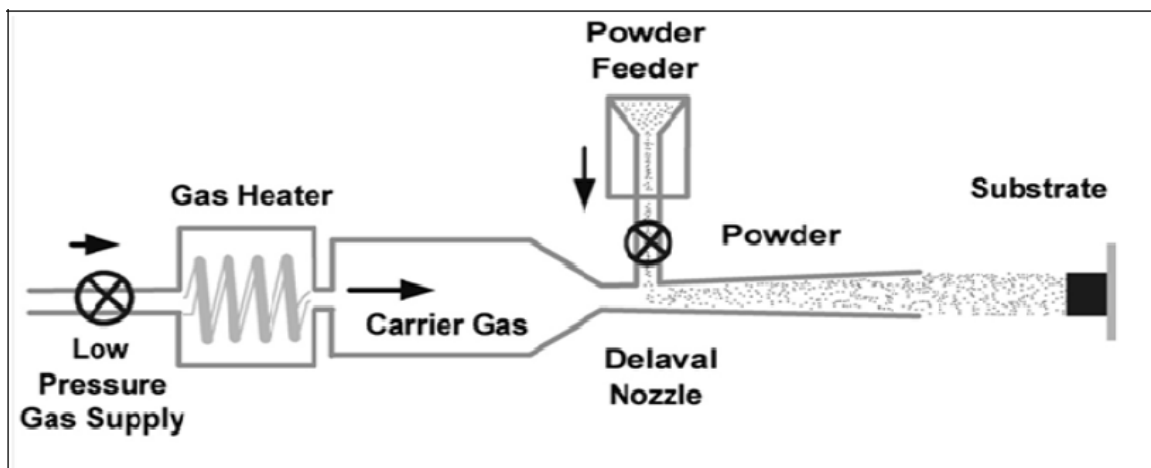


Figure 3. Diagram showing the low-pressure cold spray process, from [2].

¹ High-velocity oxygen fuel (HVOF).

While cold spray can be performed at room temperature, the pressurized gas is normally heated, usually with resistance heating, and passed through a converging-diverging (de Laval) nozzle to create a supersonic gas jet [6]. The heated gas is used primarily to further increase the speed of the gas beyond supersonic levels as the nozzle diverges. The powder particles can be heated by the gas but only to a fraction of the gas inlet temperature as the gas rapidly cools as it passes through the diverging section of the nozzle [6], [11]. In addition, the time powder particles spend in the gas flow is quite short, particularly for the low-pressure nozzle design shown in Figure 3. The increase in particle velocity as a result of heating the carrier gas can be seen in the one-dimensional MATLAB simulations in Figure 4.

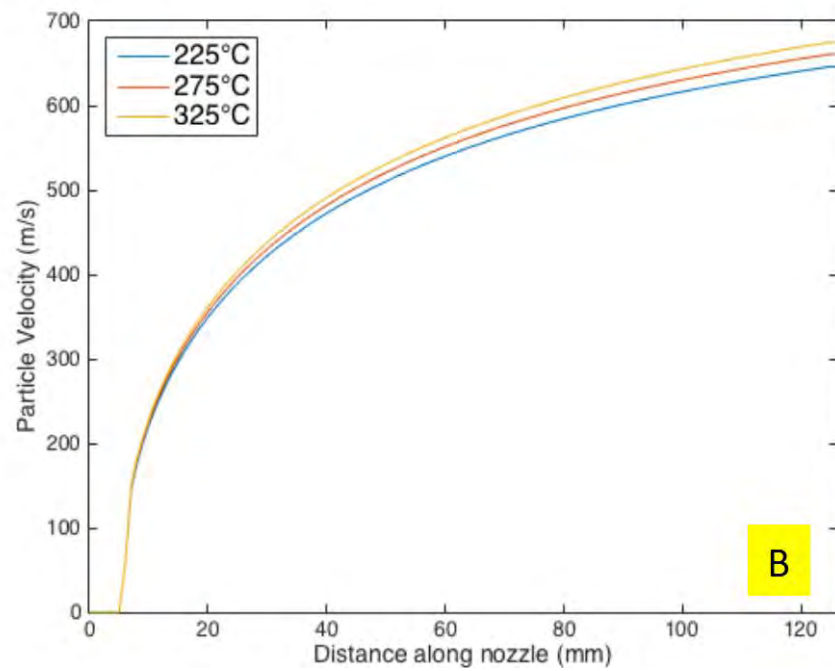
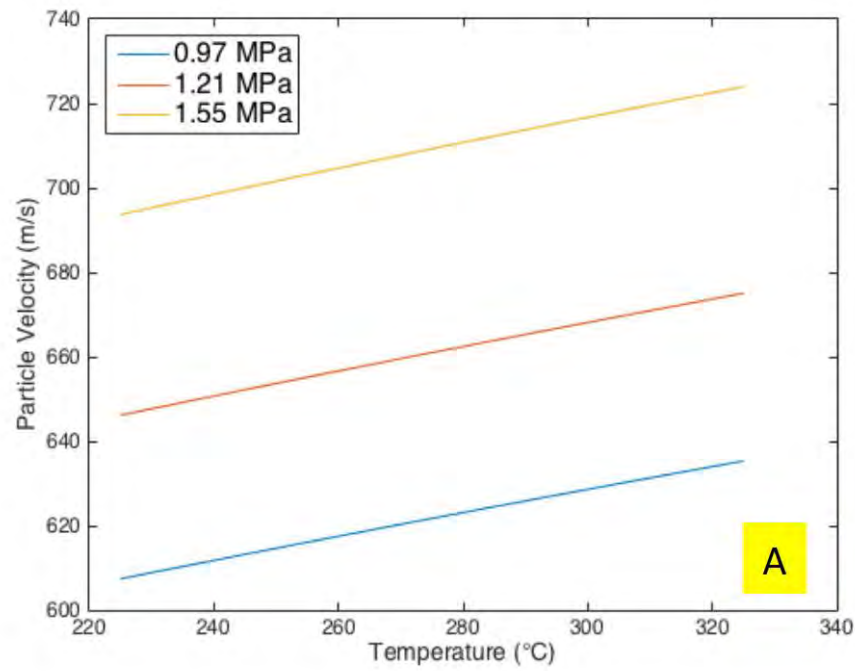


Figure 4. MATLAB simulation of: A) Particle velocity at nozzle exit as a function of carrier gas inlet temperature and pressure, and B) Particle velocity vs position in nozzle, at 1.21 MPa (175 psi), due to a change in carrier gas temperature, after [12].

Accelerating the powder particles above a certain speed is critical for deposition and adhesion to the substrate. The speed particles must achieve for deposition to occur is known as the critical velocity [7], [13], [14]. Any powder particle traveling faster than the critical velocity will deposit, while those traveling slower will peen or rebound off the substrate [15], [16]. Thus, it is imperative to understand the relationship of particle velocity to critical velocity when evaluating cold spray deposition. Gilmore et al. described the importance of particle velocity to deposition efficiency (DE) with respect to critical velocity with the spray of copper (Cu) [17]. Figure 5 shows that as particle velocity increases above critical velocity, the DE will increase. With particle velocity as the driving factor for deposition, it is imperative that the particle velocity can be accurately modeled and measured.

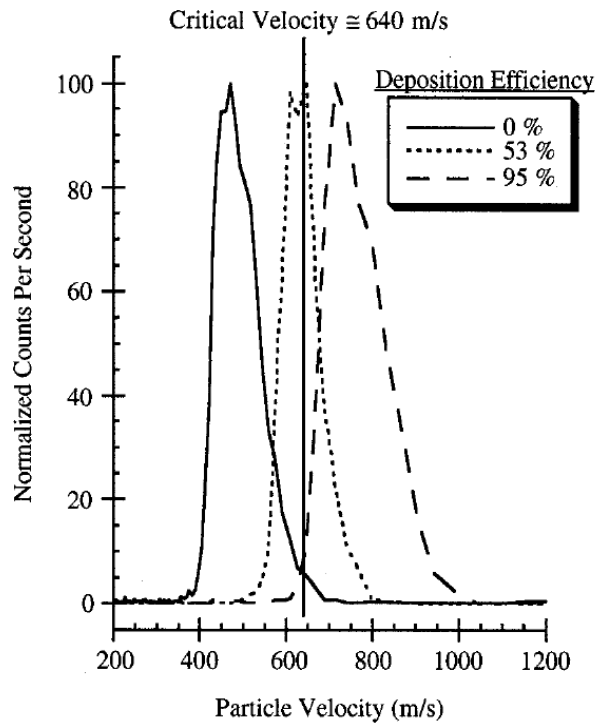


Figure 5. Particle velocity distributions for copper sprayed onto aluminum, from [17].

At a basic level, the particle velocity can be predicted using a one-dimensional approach that utilizes classic fluid dynamic equations. The gas velocity (U_{gx}) through the nozzle as a function of pressure, temperature, and gas type is represented by equation (1);

equation (2) represents the particle velocity (U_{px}) with parameters of material density, morphology, particle size, and type of gas [18]. While the gas velocity can be calculated directly for a given position in the spray nozzle, the particle velocity must be numerically integrated along the length of the spray nozzle. The particle velocity is directly proportional to the pressure and temperature of the carrier gas. An increase in either carrier gas pressure or temperature results will increase the particle velocity, and vice versa. The one-dimensional model was utilized in a MATLAB simulation (code available in the appendix) to predict particle velocity as a function of pressure (Figure 6A) and as a function of position in the nozzle (Figure 6B).

$$U_{gx} = \sqrt{2 \frac{\gamma}{\gamma-1} R T_{gi} \left[1 - \left(\frac{P_x}{P_i} \right)^{\frac{\gamma-1}{\gamma}} \right] + U_{gi}^2} \quad (1)$$

$$\frac{dU_{px}}{dt} = \frac{3 C_d \rho_{gx}}{4 D_p \rho_p} (U_{gx} - U_{px}) |U_{gx} - U_{px}| \quad (2)$$

where:

- U_{gx} : gas velocity at any point, x, along the nozzle
- R : gas specific constant
- T_{gi} : inlet temperature of the working gas
- P_x : gas pressure at any point x along the nozzle
- P_i : inlet gas pressure
- γ : specific heat ratio of the working gas
- U_{gi} : inlet gas velocity
- U_{px} : particle velocity at any point, x, along the axis of the nozzle
- C_d : drag coefficient for a sphere, is a function of particle Reynolds number
- D_p : particle diameter
- ρ_{gx} : gas density at any point, x, along the nozzle that varies with the temperature and pressure of the gas
- ρ_p : particle density

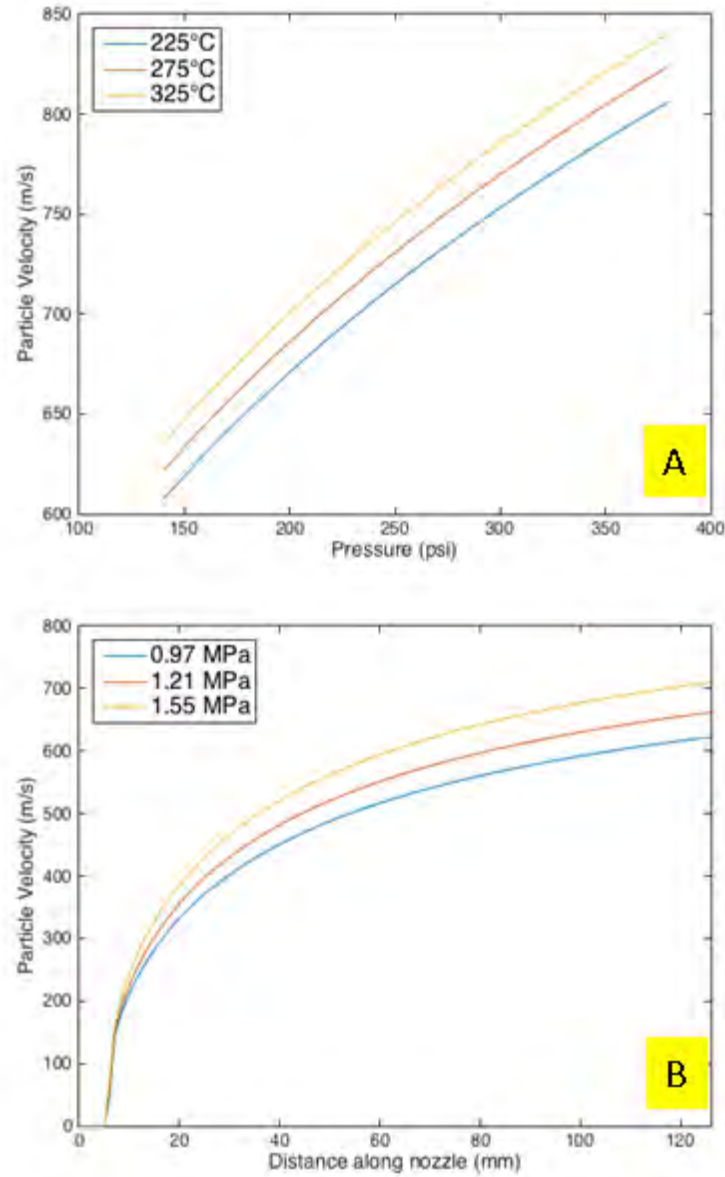


Figure 6. MATLAB simulation utilizing the one-dimensional fluid dynamics equations for A) particle velocity at the nozzle exit as a function of temperature and pressure, and B) particle velocity versus position in the nozzle, at 275°C, at a given pressure, after [12].

Equations 1 and 2 are valid for the velocities in the nozzle but do not predict velocity at the point of deposition, which is several millimeters beyond the nozzle exit. Understanding the fluid dynamics used to model particle velocity is critical for determining the critical velocity for a given standoff distance. The use of similar fluid dynamics equations has been used to further investigate flight characteristics of the high

velocity powder to calculate critical velocity [19]. The previously calculated parameters were used with calculated values of deposition efficiency (DE) and coating strength to produce parameter selection maps that show the ideal conditions for conducting cold spray [19]. The parameter selection maps are useful as they allow a user to choose ideal spray conditions based on their spray material and desired coating without having a thorough understanding of fluid mechanics. The MATLAB simulation predictions (Figure 6) are accurate assuming no effect of bow shock from outside the nozzle. It has been demonstrated that bow shock can have a significant effect on particle and gas velocity as well as DE [20]. There are three distinct regions of bow shock: (1) the small standoff region, where the bow shock adversely affects the DE; (2) the medium standoff region, where the bow shock has disappeared and as long as carrier gas velocity is above particle velocity the DE increases; and (3) the large standoff region, where the particles decelerate since the carrier gas velocity is no longer greater than particle velocity [20].

Computational fluid dynamics (CFD) can also be used to predict the in-flight particle velocity and temperature as a function of spray parameters. CFD has recently been used to model the phenomenon in two dimensions [13]. In a comparison between the CFD and one-dimensional model of particle velocity versus distance from the nozzle inlet, the results were close considering the different equation sets utilized (see Figure 7) [13]. The CFD results showed slightly lower carrier gas and particle velocities as a result of viscous effects such as boundary layer. The oscillations found in the CFD results represent flow separation and shock/expansion waves near the end of the nozzle. The bow shock has a standoff of approximately 1mm that causes the carrier gas velocity to rapidly approach zero when the standoff distance is reached.

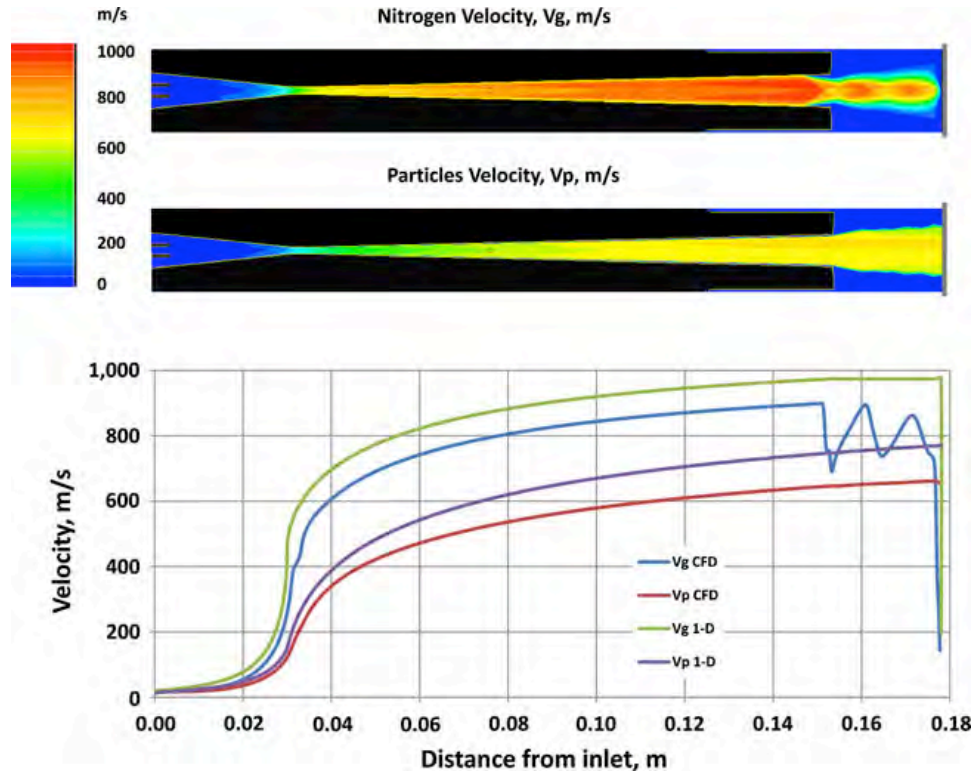


Figure 7. 1-D and CFD calculated results of accelerating aluminum particles with nitrogen, from [13].

While particle velocity is an important variable for cold spray deposition, feed stock powder characteristics are just as vital. There are many variables that affect deposition such as particle size, morphology, material, and how the particles are processed. Among the variable parameters, the particle size is the most controllable while morphology is the least controllable [21]. It has been shown that a particle size range of 10–50 μm in diameter is ideal for cold spray deposition [16], [22]–[24]. Particles $<5 \mu\text{m}$ are difficult to feed properly and lose velocity downstream of the bow shock while particles $>50 \mu\text{m}$ have too much inertia to accelerate above the critical velocity [24]. The smaller particles are easily accelerated since the particle acceleration imparted by the gas is proportional to $1/d$, where d is the diameter [23]. The shape of the particle also had an effect of the velocity. Larger non-spherical powders experience higher velocities than spherical particles due to having a higher drag coefficient [16], [23], [24]. As seen in Equation 3, the drag force of the particle is proportional to the drag coefficient, therefore an increase in drag coefficient from a non-spherical particle results in a higher drag force

and a higher velocity [23]. Though high velocities have been obtained for various shapes, the optimal shape for cold spray is still an area that is being studied.

$$D = \frac{1}{2} \rho V_{rel}^2 A_p C_d \quad (3)$$

where:

D: drag force

ρ : propellant gas mass density

V_{rel} : relative velocity between the propellant gas and the particle

A_p : particle projected surface area

C_d : drag coefficient

2. Utilizing Aluminum Alloy Powder in the Cold Spray Deposition Process

There has been an increase in the scientific literature for cold spray deposition of various aluminum alloys. The use of CP-aluminum, HP-aluminum and various aluminum alloys as corrosion protection coatings were studied as these powders were deposited on magnesium alloy gear boxes of UH-60 Seahawk helicopters [4]. The pure aluminum coatings of thickness ~ 0.38 mm proved to be an effective corrosion barrier in electrochemical polarization and salt-spray testing [4]. The HP-aluminum coating was effective at resisting galvanic corrosion as it showed no effects from testing while the CP-aluminum and aluminum alloy coatings had galvanic currents up to 50 times greater than HP-aluminum [4]. The deposits of these alloys proved to be excellent barriers to prevent corrosion and also allowed the dimensional restoration of material on the gearbox.

Recent work in Australia has begun to extend cold spray repair to the higher strength alloy, AA7075. The work of N. Matthews et al. [25] and R. Jones et al. [26] developed a coating that could be used in repairs to prevent future aircraft from meeting a fate similar to the Aloha aircraft failure in 1988, NSTB 89-03. Recently AA7075, a heat treatable alloy with high fatigue strength, was sprayed on AA2024 substrate as a structural repair option for aircraft structures [25], [26]. When applied to fasteners, 1 mm thick spray coatings of AA7075 were shown to increase the fatigue life of the joint by a factor of 3 [25]. The cold spray deposit of AA7075 can also be used to repair corrosion damage while increasing fatigue life of the repaired component. During fatigue testing,

the corrosion repairs using cold spray displayed an average fatigue life of 15 million cycles compared to approximately 36,000 cycles of traditionally repaired components [26]. Cold spray of 7075 also proved successful in the repair of multi-site damage without creating more stresses or over hardening the surrounding areas [25], [26].

R. Ghelichi et al. [27] also studied the effects of fatigue behavior after the spray of AA7075 powder. In their experiments, AA5052 substrates were sprayed with pure Al and AA7075 and analyzed residual stresses, hardness, and fatigue behavior. The AA7075 sprayed samples were found to have a hardness of almost twice that of the substrate [27]. As a result of the cold spray process, compressive residual stresses were found in the substrate surface and deposited material. The compressive residual stresses led to an increase in the fatigue life of up to 30% in all samples sprayed with AA7075 [27].

The microstructure of ultra fine grained particles was studied in the cold spray of heat treatable AA6061. Utilizing BSE imaging, the as-atomized powder was seen to have the same grain structure on the surface as in the center of the particle. Energy dispersive spectroscopy (EDS) analysis showed that the grain boundaries are rich in Si, Mg, Cu, and Fe due to solute segregation. The cold sprayed deposit was studied using a heat treatment of 10°C/minute to 450°C to allow for full recovery, recrystallization, and grain growth of the microstructure [28].

The utilization of aluminum-copper alloys (2xxx series) is extremely common in the aerospace industry due to its good strength-to-weight ratio. The 2xxx series alloys contain copper as the primary alloying element that adds strength by precipitation hardening. Precipitation hardening adds strength to the alloy without significantly increasing the density. Unfortunately, the 2xxx series alloys are quite susceptible to corrosion. High strength in the precipitation-hardened condition makes the alloy susceptible to stress corrosion cracking while copper corrosion products deposit on the surface and create a galvanic cell [29]. The susceptibility to corrosion leads to 2xxx series alloys being used in conjunction with a corrosion resistant coating. With its high strength and resistance to fatigue, AA2024 is used to provide structural support to vital parts of an aircraft such as the wing and fuselage supports [30]. Despite its importance, the AA2xxx series of alloys have received little attention in the cold spray literature. Ajdelsztajn et al.

[31] has demonstrated cold spray deposition of AA2618, but cold spray of AA2024 or AA2014 has not been reported. It is imperative that these alloys are studied so the mechanisms during cold spray can be understood and a repair process can be implemented.

Despite the growing knowledge base on cold spray of aluminum alloys, we still do not have a systematic understanding of how alloying additions affect the spray process and the microstructure of the deposited material. Just as important, we do not have a comprehensive understanding of how alloy additions affect the microstructure of the feed-stock powders, the key variable to control deposition efficiency and coating properties. This thesis will address how copper alloying additions in the Al-Cu system change the microstructure of the powders, the spray characteristics of the powder, and the resultant microstructure and properties of the cold spray deposited material.

C. OBJECTIVES

(1) Characterize binary Al-Cu alloy powders

We will use a series of Al-Cu binary alloy powders, produced by gas atomization, containing 2–5 wt% copper and characterize them for size, composition, phase content, crystallite size, and mechanical properties. The as-received powders are likely to contain an Al_2Cu phase, which will be critical in controlling the strength of the powder particles. The relationship between particle size, shape, and microstructure will be investigated.

(2) Produce cold spray coatings using Al-Cu alloy powders

We will conduct cold spray deposition experiments for each of the powders while varying temperatures and pressures to determine the correlation between spray conditions and DE. As our central goal in this objective is to assess how changes in powder composition and microstructure affect cold spray deposition, we will only change the temperature and pressure during the spray. The spray gun geometry, the standoff distance, the powder feed rate, type of gas (He), and the substrate (roughness and temperature) will remain fixed. Through deposition experiments and laser velocimetry, we will attempt to measure the in-flight characteristics of the powders and attempt to measure a critical velocity as a function of copper content.

- (3) Investigate the basic microstructure-mechanical property relationships for cold spray deposited Al-Cu alloy coatings

The microstructure of the deposited materials will be characterized to determine the effects of powder composition and processing parameters on coating thickness, hardness, and DE. Metallographic sections will be produced and will be examined by optical microscopy and scanning electron microscopy (SEM) to examine the porosity and grain size of the deposited materials. In particular, the substrate-deposit interface will be examined in detail as the quality of this interface strongly affects adhesion, a key quality of a good repair.

THIS PAGE INTENTIONALLY LEFT BLANK

II. EXPERIMENTAL METHODS

A. POWDER PRODUCTION

Valimet, Inc. from Stockton, California produced four Al-Cu binary alloys with 2, 3, 4, and 5 wt% copper. This powder was characterized for composition, phase content, mechanical properties and was used for deposition in cold spray experiments. The powders were produced by gas atomization using nitrogen as the inert gas. The gas atomization produced approximately 90 pounds of each powder at a median particle size of 20 μm , which is an ideal range for cold spray. To verify the composition of the produced powders, Anamet, Inc. was contracted to perform a light element analysis of copper, oxygen, nitrogen, silicon and carbon. The light element analysis was completed by LECO combustion and direct current plasma atomic emission spectroscopy (ICP-AES), with the results in Table 1 showing that the powders produced are comprised almost entirely of aluminum and copper and that the copper content of the each powder is within the ordered specification.

Table 1. Light element analysis of the Al-Cu binary powders produced from gas atomization with nitrogen gas.

| <u>CHEMICAL ANALYSIS - DCP</u> (Reported as Wt. %) | | | | | | |
|---|------|--------|--------|--------|--------|-------------|
| | | 2% Cu | 3% Cu | 4% Cu | 5% Cu | Error |
| Carbon* | (C) | 0.005 | 0.004 | 0.003 | 0.003 | ± 0.001 |
| Copper | (Cu) | 2.16 | 3.06 | 3.98 | 5.16 | ± 0.2 |
| Nitrogen* | (N) | <0.005 | <0.005 | <0.005 | <0.005 | ± 0.001 |
| Oxygen* | (O) | 0.25 | 0.19 | 0.2 | 0.24 | ± 0.02 |
| Silicon | (Si) | 0.04 | 0.037 | 0.038 | 0.041 | ± 0.002 |
| *Determined by LECO combustion | | | | | | |

The only modification to the powder was a heat treatment of 200°C for 11 hours applied for a particular x-ray diffraction experiment; otherwise, the powders were used and analyzed in an as-received condition.

B. POWDER CHARACTERIZATION

(1) Particle Analysis

The Horiba Laser Scattering Particle Size Analyzer (LA-950V2) was used to measure the particle size distribution of the powders. To measure the particle size distribution, approximately 500 mg of each powder was placed in a test cell filled with isopropanol.

(2) Sample Preparation of Al-Cu Powders and Coatings

To prepare the Al-Cu powders for metallographic analysis, they were mixed with Struers EpoFix and cold mounted. The Al-Cu coatings were hot compression mounted in Buehler Konductomet powder. Following standard metallographic preparation techniques, grinding was performed on the samples with sand paper starting at 800 grit and finishing with 2400 grit. The samples were then polished with Buehler Ecomet polishing machines on Buehler microcloths using 3 μm and 1 μm alumina oxide. The final polishing of the samples was performed on a Buehler Vibromet2 Vibratory Polisher with a 0.05 μm colloidal silica-polishing compound for approximately four hours. For analysis in the SEM, the samples were coated with approximately 3 nm of platinum-20 palladium using a Cressington 208HR sputter coater.

(3) Scanning Electron Microscopy for Powder and Coatings

A Zeiss Neon 40 FE-SEM at 15 keV with a 60 μm objective aperture and a nominal electron probe current of 1120 pA was used to capture in-lens secondary electron (ILSE) and backscatter electron (BSE) images of the powders. BSE images of the powders were analyzed using the ImageJ software to measure the cellular spacing of particles with cross section diameters between 15 and 30 μm . To obtain the average cellular spacing for each composition, approximately 10 measurements were made on at least 100 particles of each powder. The EDAX Pegasus energy dispersive x-ray spectroscopy (EDX) system connected to the SEM was used for compositional quantification, x-ray mapping, and line scans of each powder. The EDX maps were collected with the SEM at 20 keV, an objective aperture of 120 μm , a dwell time of 200 μs , a pixel ratio of 0.297 microns per pixel and an image size of 256x200 pixels. The

quantification of elements was performed with the SEM at 20 keV, a working distance of 5 mm, and an objective aperture of 60 μm . Quantitative analyses of all spectra in this study were carried out applying ZAF correction and using standards of pure element samples of Al and Cu.

(4) X-ray Diffraction

X-ray diffraction (XRD) was performed to determine volume fraction and lattice parameters of the annealed and as-received powders. A Rigaku Miniflex 600 diffractometer with Cu K α radiation source at 40 kV and 15 mA with a D/teX Ultra detector was utilized to perform XRD. Diffraction data was collected using a 2θ scan axis with a step width of 0.02° and a scan speed of 5 degrees/minute across an 18–120° scan range for all analysis. The volume fraction and lattice parameters were determined through a Rietveld refinement approach using the Bruker-Topas software that utilized ICDD database cards 04-017-5200 and 04-001-0923. In a second set of measurements, samples of all four powders were annealed at 200°C for 11 hours to allow the powders to approach their equilibrium microstructure. The XRD results of the annealed powders were then compared to the results of the as-received powders.

C. COATING PRODUCTION

1. Cold Spray Deposition Experiments

The Centerline SST Model Series C low-pressure cold spray system (see Figure 8) was utilized for the deposition experiments. The system used a polymer nozzle with a 120 mm divergent barrel and a 2 mm throat at a standoff distance of 12 mm to the substrate. The standoff distance was measured from the bottom of the nozzle to the substrate surface. Prior to any sprays, the powders were placed in an oven at 60°C for approximately 12 hours. This drove off any moisture that may have absorbed and prevented the powder from clumping in the vibrational hopper of the cold spray unit. The powders were then sprayed onto aluminum 2024-T3 substrates, heated to approximately 200°C via a heat tape, that were grit blasted prior to deposition. The substrates were grit blasted with Centerline SST-G002 alumina grit powder at a feed rate of 30%, nitrogen gas at 0.48 MPa (70 psi) and 25°C, a step size of 2.4 mm, and a standoff distance of 5

mm. During powder deposition, the step size and standoff distance were reduced to 1.2 mm and 12 mm respectively and helium was used at various pressures and temperatures. The deposition conditions are shown in Table 2.



Figure 8. Centerline SST Model Series C low-pressure cold spray system installed at the Naval Postgraduate School.

Table 2. Conditions used in the cold spray deposition experiments.

| Powder (Al-Cu with varying wt% of Cu) | 2%, 3%, 4%, 5% |
|--|--|
| Gas | He |
| Substrate Material | AA2024 |
| Gun Type | Automatic |
| Nozzle | Polymer |
| Gas Temperature (°C) | 225, 275, 325 |
| Gas Pressure (Mpa) | 0.97 (140 psi), 1.21 (175 psi), 1.55 (225 psi) |
| Nominal Powder Feed Rate (%) | 30 |
| Stand Off Distance (mm) | 12 |
| Gun Speed (mm/s) | 40 |
| Gun Step Size (mm) | 1.2 |

After the spray experiments, DE and deposition thickness were measured. To account for the different actual feed rates of the cold spray unit, the DE was measured by taking a ratio of mass of powder deposited to the mass of powder sprayed. This can be seen in the following equation

$$DE(\%) = \frac{Mass_{substrate\ final} - Mass_{substrate\ initial}}{Mass_{powder\ initial} - Mass_{powder\ final}} \times 100\% \quad (4)$$

The mass of the substrate was measured after grit blasting and again after deposition of the powders. The mass of the powders was measured prior to being loaded for spray and at the completion of the spray. All masses were measured using a digital scale that is accurate to 0.0001 g. The thickness of the spray deposition was measured at the center of the deposition with a digital micrometer accurate to 0.01 mm (0.0001 in).

2. Particle Velocity Experiments

The 2 and 5 wt% copper powders were selected for the measurement of in-flight velocity due to these powders having the largest variations of Cu content. With cold spray being lower temperature than traditional thermal spray, a laser is utilized since there is not enough heat radiated to support thermal imaging. To measure the velocity of the particles, the TECNAR Automation CSM eVOLUTION was utilized. The CSM eVOLUTION provides real-time monitoring of parameters (velocity and diameter of particles) of the particle plume itself [32]. The CSM eVOLUTION uses a dual slit optical device in order to perform in-flight diagnostics on individual particles while providing

simultaneous and precise velocity and diameter measurements of up to 800 individual particles/s depending on spraying conditions [32].

To measure the particle velocities the sensing head was set 60 mm from the center of the nozzle with the laser alignment dots set at the nozzle tip as seen in Figure 9. Then each powder was sprayed, according to the conditions in Table 3, and velocity was measured by the TECNAR for 20 seconds. The measured velocities were then tabulated and plotted for use in the critical velocity calculation.

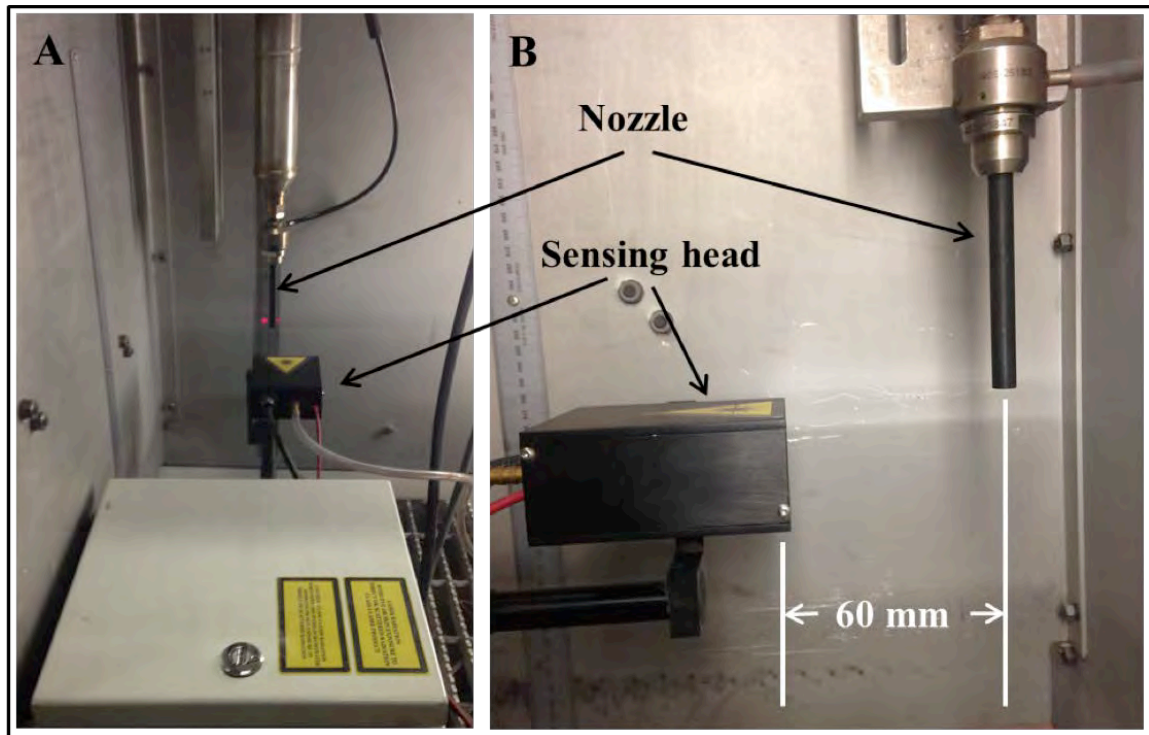


Figure 9. Tecnar setup for the particle velocity experiment showing A) rear view, and B) side view. Image from [12].

Table 3. Combination of the pressures and temperatures used for velocity and deposition sprays. All other conditions were held the same.

| | | Temperature (°C) | | |
|----------|-----------------------|------------------|-------|-------|
| | | 225°C | 275°C | 325°C |
| Pressure | 0.97 Mpa (140 psi) | | X | |
| | 1.21 Mpa (175 psi) | X | X | X |
| | 1.55 Mpa (225 psi) | | X | |

The critical velocity was then calculated using the DE from the deposition sprays and the measured velocities for each spray condition. The right side of the velocity profile is 100% volume fraction. Using the assumption that only the particles moving faster or equal to critical velocity will result in deposition, the critical velocity is found by numerically integrating the area under the velocity curve until that area matched the DE for a given deposition experiment (see Figure 10). In Figure 10, the area under the curve (yellow) represents the fraction of particles with a velocity above the assumed critical velocity. DE is the deposition that corresponds to this particle velocity distribution. Critical velocity was calculated for the 2 and 5 wt% copper powders sprayed at the conditions in Table 3.

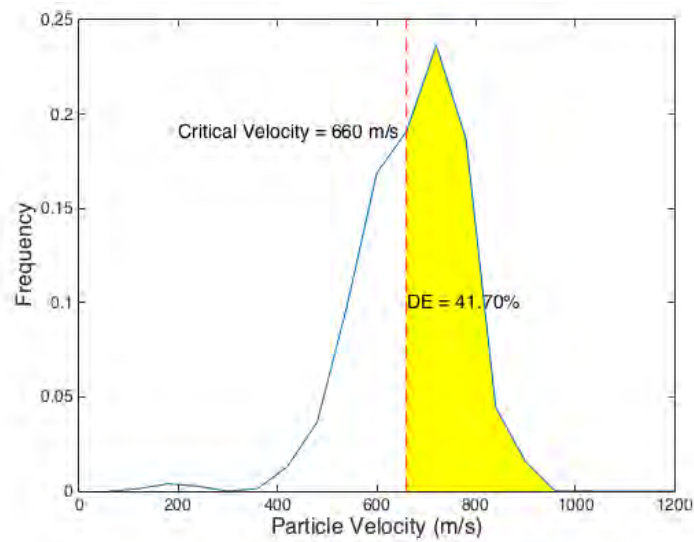


Figure 10. Critical velocity as it is calculated using DE.

3. One-Dimensional MATLAB Simulation of Centerline SST Model Series C UltiLife Nozzle

To investigate the gas dynamic process and particle transport properties during the cold spray experiments, the one-dimensional MATLAB simulation model of the Centerline nozzle developed by Jonathan Schiel was utilized (code available in the appendix) [12]. This model is based upon the calculations of K. Sakaki in chapter 7 of *The Cold Spray Materials Deposition Process*, edited by V.K. Champagne [18]. The simulations were completed to compare the simulated particle exit velocities versus the measured particle exit velocities. In this model, the parameters of gas pressure, gas temperature, particle cross-section, and particle density were varied to obtain particle exit velocity. The 2 and 5 wt% Cu powders were selected for the simulation to compare directly to the measured laser velocimetry with densities of $2,826 \text{ kg/m}^3$ and $3,015 \text{ kg/m}^3$ respectively. The simulated parameters of temperature and pressure were varied as in Table 3 to match the velocimetry sprays for further study of particle exit velocity. After setting the simulated gas temperature and pressure, the particle sizes obtained from the Horiba particle sizing experiment were utilized to obtain simulated particle exit velocities.

4. Hardness

A Mitutoyo micro vickers hardness tester was used to obtain micro-hardness data for the cold spray applied deposits and AA2024 substrates. A force of 100 grams was used with a dwell time of 18.5 seconds. Each coating and substrate was sampled three times and an average hardness value was calculated from those values.

III. RESULTS

A. POWDER CHARACTERISTICS

The powders were characterized to determine the effects of systematically increasing the alloying agent on the microstructural parameters in the starting powder. The binary Al-Cu powders were then assessed for the potential for cold spray repair of 2xxx series aluminum alloys.

1. Particle Sizing

The particle sizes of the powders all show a similar Gaussian distribution as seen in Figure 11. The powders are sized accordingly to the order specification placed with Valimet, Inc. The mean particle size for the powders is between 22–26 μm (Table 4), making the particles suitable for cold spray deposition. The range of powder sizes can be seen in Figure 11. The particle size distribution did not differ meaningfully as a function of copper content.

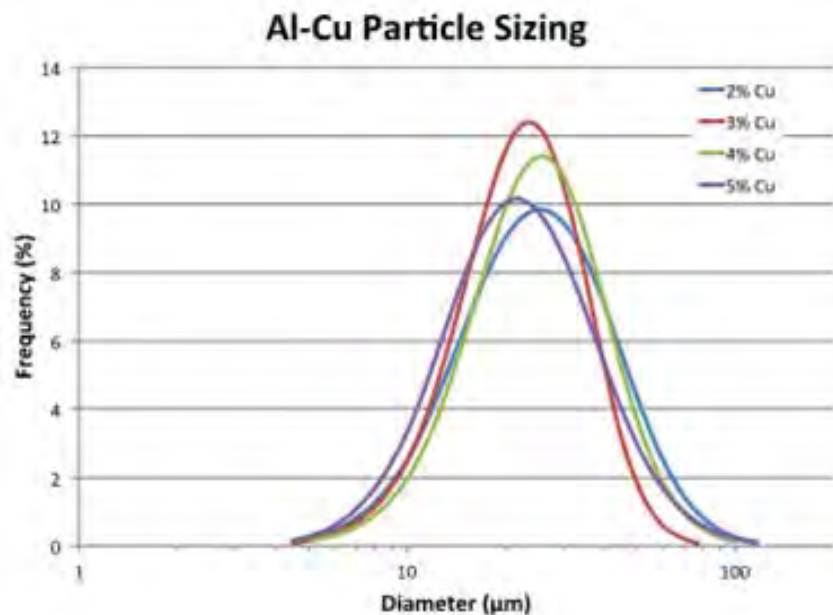


Figure 11. Particle sized distributions for the Al-Cu powders received from Valimet, Inc.

Table 4. Al-Cu particle size characteristics.

| Wt % Cu | Median size (μm) | D10 (μm) | D90 (μm) |
|----------------|---|---------------------------------------|---------------------------------------|
| 2 | 26.31 | 11.28 | 45.31 |
| 3 | 22.50 | 11.46 | 35.55 |
| 4 | 25.75 | 12.24 | 42.27 |
| 5 | 23.68 | 10.34 | 40.83 |

2. Particle Morphology

The morphology and shape of the powders are consistent with powders produced from gas atomization [21], [33], [34]. The spherical shape of the powders, as can be seen in Figure 12, is due to the properties of the molten metal as it leaves the atomizer nozzle during gas atomization [34]. The spherical shape of the particles will simplify the modeling in the MATLAB simulation, thus eliminating the need to apply a correction factor for a non-spherical shape. The powders show a nearly smooth surface with depression at the cell boundaries clearly displaying cellular solidification. Cellular solidification is a product of gas atomization as the particles experience a very high cooling rate, $\sim 11,000$ K/s, that does not allow for the growth of dendritic arms [34], [35].

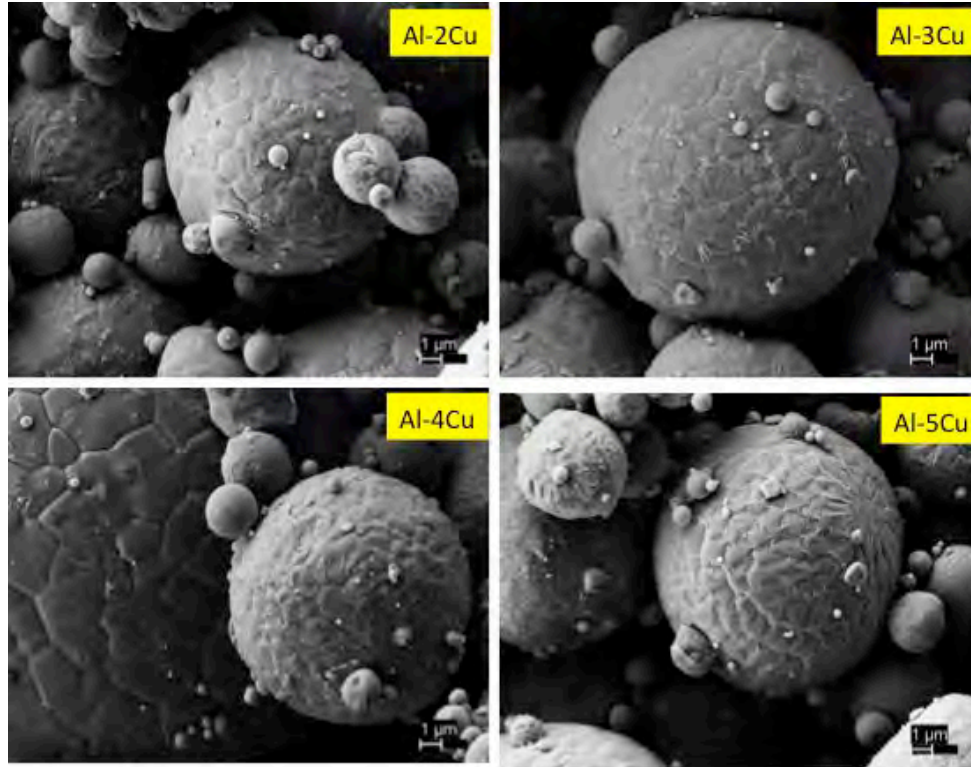


Figure 12. Secondary electron images of the Al-Cu powders as received.

The as-received powders show a cellular microstructure with copper rich cell boundaries areas (appearing bright due to the higher average atomic number) clearly visible in the BSE micrographs (Figure 13). It can be seen in all of the powders that both the ILSE and BSE imaging techniques show the Cu rich boundaries that are formed during the rapid cooling during gas atomization. While both techniques allow for the measurement of the cellular spacing, the BSE images provide clearer images of the Cu rich boundaries and were utilized for measurements. This approach is contrary to an experiment performed by Mullis et al. [36], where the etched SE images were used to perform measurements of the secondary dendrite arm spacing of Al-4 wt pct Cu powders as etching tends to attack the boundary areas preferentially, leading to increased errors in measurement. The darker regions of the particles are areas of preferential etching of material that occurred during metallographic preparation.

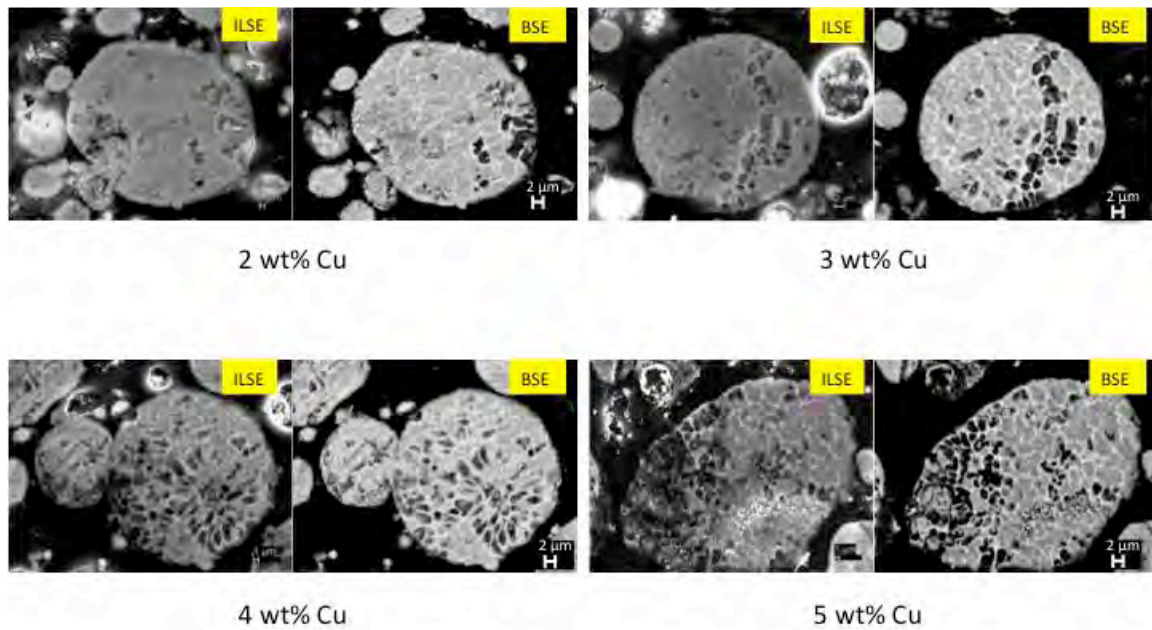


Figure 13. ILSE and BSE images of the as-received powders at 2000x magnification.

It can clearly be seen that the 3, 4, and 5 wt% powders display cellular solidification. The cellular structure in the 2 wt% powder is not as well defined as the other powders due to the low amount of Cu (Figure 14) and hence the lower volume fraction of Al_2Cu . The solidification microstructure is a result of the wt% Cu in the powders. The apparent variations in particle diameters observed in these polished samples are due to the sectioning effect and the largest diameters only are representative of actual particle sizes. The fact that the cell size in various sections appear to be the same suggests that the cell size is quite uniform within the powder particles.

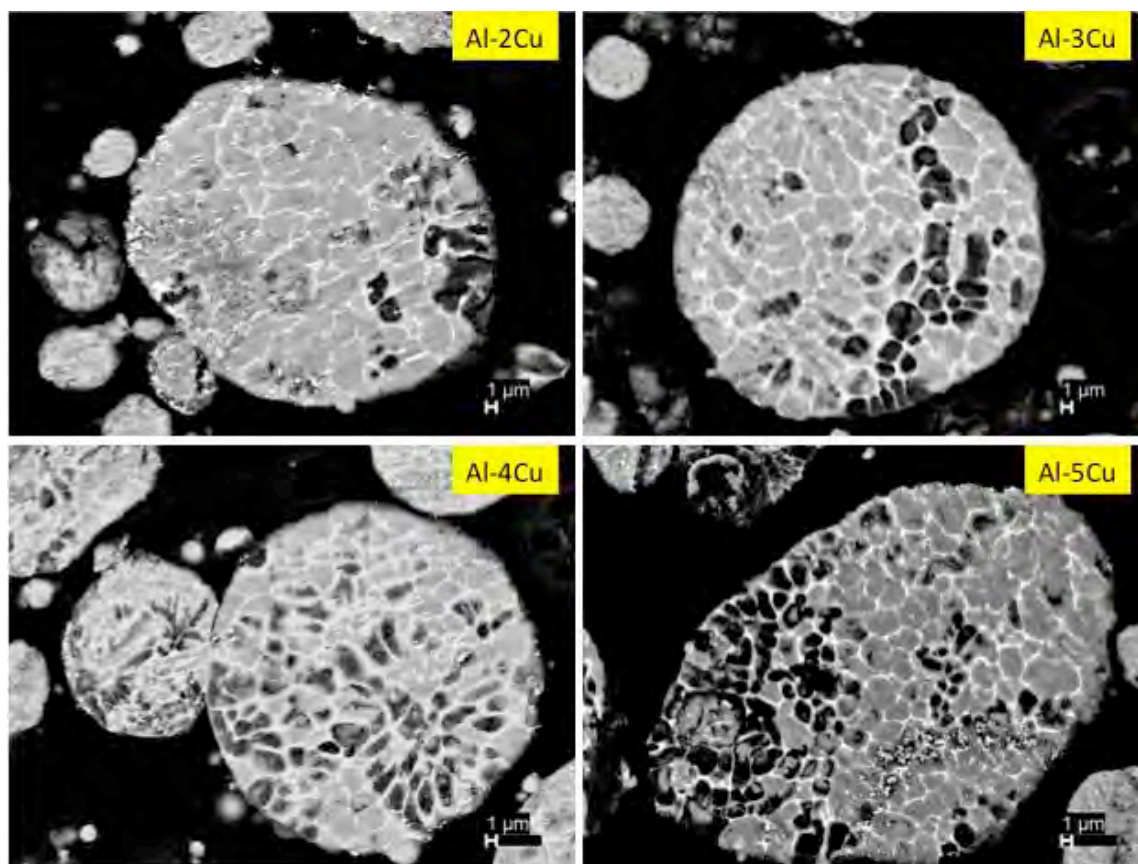


Figure 14. Backscatter images of the as-received powders. The cellular structure is similar for all of the powders except the Al-2Cu wt%.

Cellular spacing measurements of the as-received powders showed some measurable variance. The average cellular spacing varied little between the powders, 1.58-1.96 μm , with the Al-2Cu and Al-3Cu powders having the largest spacing. The data suggests a decreasing trend in cellular spacing as the wt% of copper increases as seen in Figure 15, although the standard deviation surrounding the mean does not show a statistically significant trend. The change in cell spacing with increasing copper content is more clearly displayed by examining the total distribution of cell sizes for each composition (Figure 16). The cell size distributions show that the powders with the higher copper content have a higher frequency of a smaller cellular spacing. Lastly, in the Al-4Cu and Al-5Cu powders there are more cells per particle than the Al-2Cu and Al-3Cu powders. The range of the cellular spacing also decreases as the copper content increases (Table 5). It appears that the cellular formation is due to the high cooling rate from gas atomization while the spacing is possibly a function of copper content.

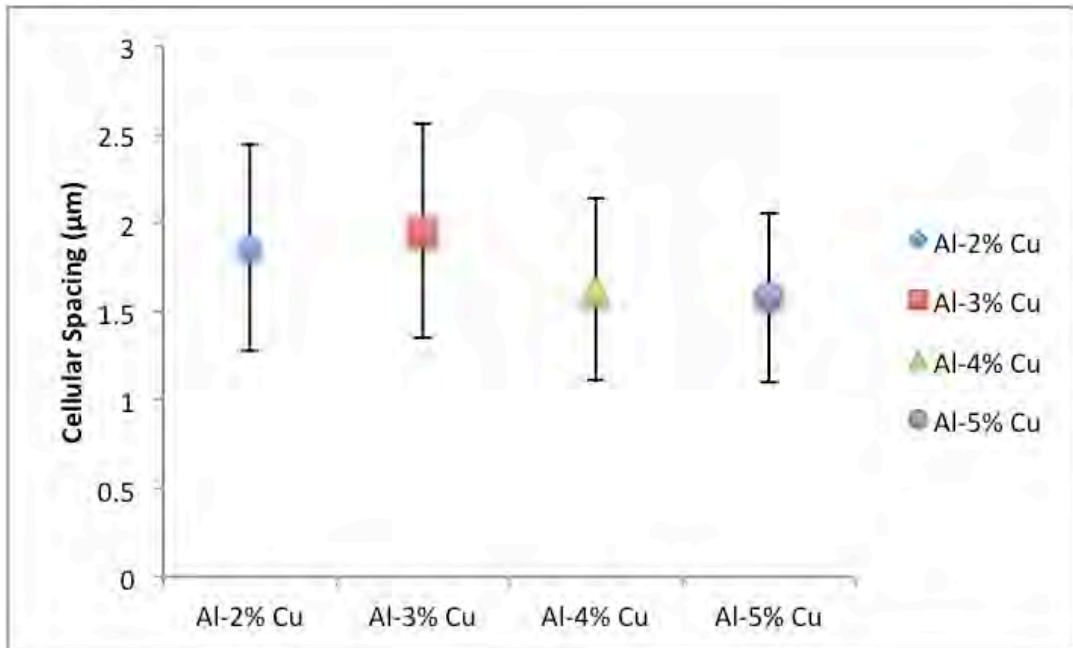


Figure 15. Average cellular spacing of the as-received powders with cross sections between 15–30 μm .

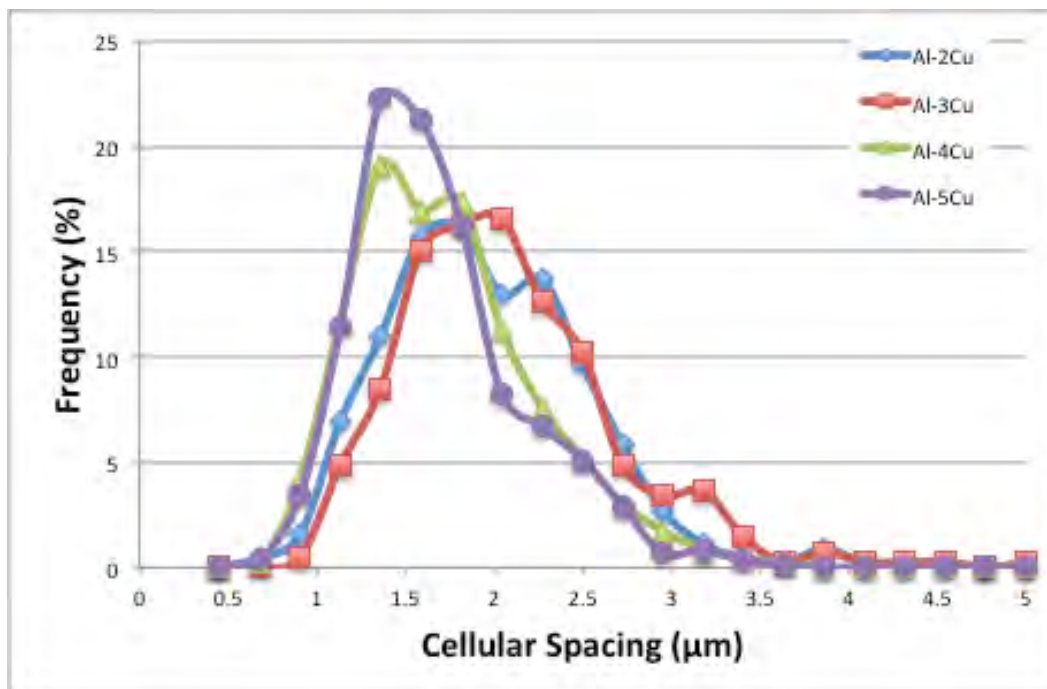


Figure 16. Graph representing the frequency of the measured cellular spacing for the as-received powders.

Table 5. Cellular spacing characteristics of the as-received powders.

| wt% Cu | Average Cellular Spacing (μm) | Cellular Spacing Standard Deviation (μm) |
|--------|--|---|
| 2 | 1.85 | 0.58 |
| 3 | 1.96 | 0.61 |
| 4 | 1.62 | 0.51 |
| 5 | 1.58 | 0.48 |

3. EDS Quantification

EDS spectra analysis (Figure 17) and quantification (Figure 18) of the Al-5Cu powders show that the cell boundaries have a greater wt% of copper when compared to the center of the adjacent cells. The EDS spectrum in Figure 17 also shows platinum (Pt) from the sputter coating applied to the sample. Carbon (C) and oxygen (O) were introduced during the cold spray deposition and appear in the spectra analysis. Three points, one at the center of the cell boundary and the others at the center of the two adjoining cells, marked in Figure 18, were analyzed. The amount of copper at the cell boundaries is greater than the wt% of copper specified for each powder (Table 6). The quantification results shown in Figure 19 indicate that there is clear copper enrichment at the cell boundaries in all of the powders but were most significant in the 4 and 5 wt% powders. The highest concentration of copper measured was 10 wt% in the 4 wt% copper powder (Figure 19). The calculated wt% Cu for the Al_2Cu phase is 53.7 wt%. The calculated wt% Cu for Al_2Cu is different than the wt% Cu measured at the cell boundaries due to the size of the probe, which is measuring both Al_2Cu particles and the surrounding Al matrix. What is being reported from the EDS measurement is an average of the Al and Al_2Cu particles. It is also interesting to note that there appears to be some iron enrichment at the cell boundaries. Based on Figure 18, it appears that iron concentrates at the cell boundaries.

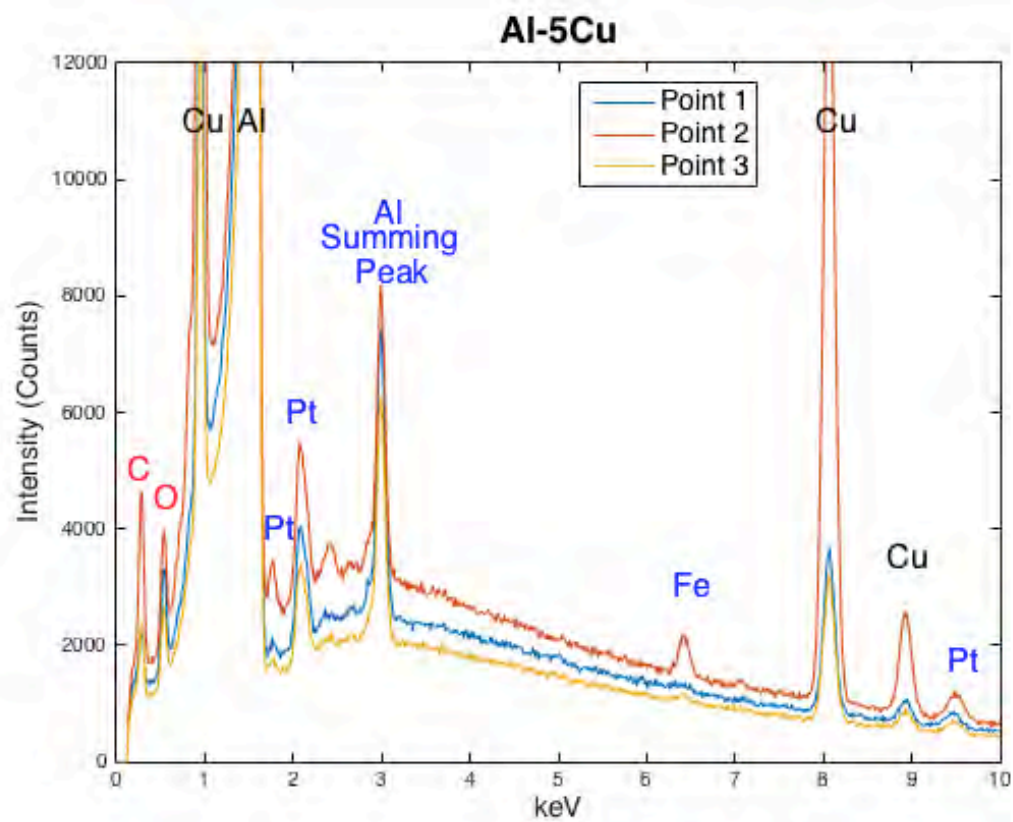


Figure 17. EDS point spectra for Al-5Cu powder.

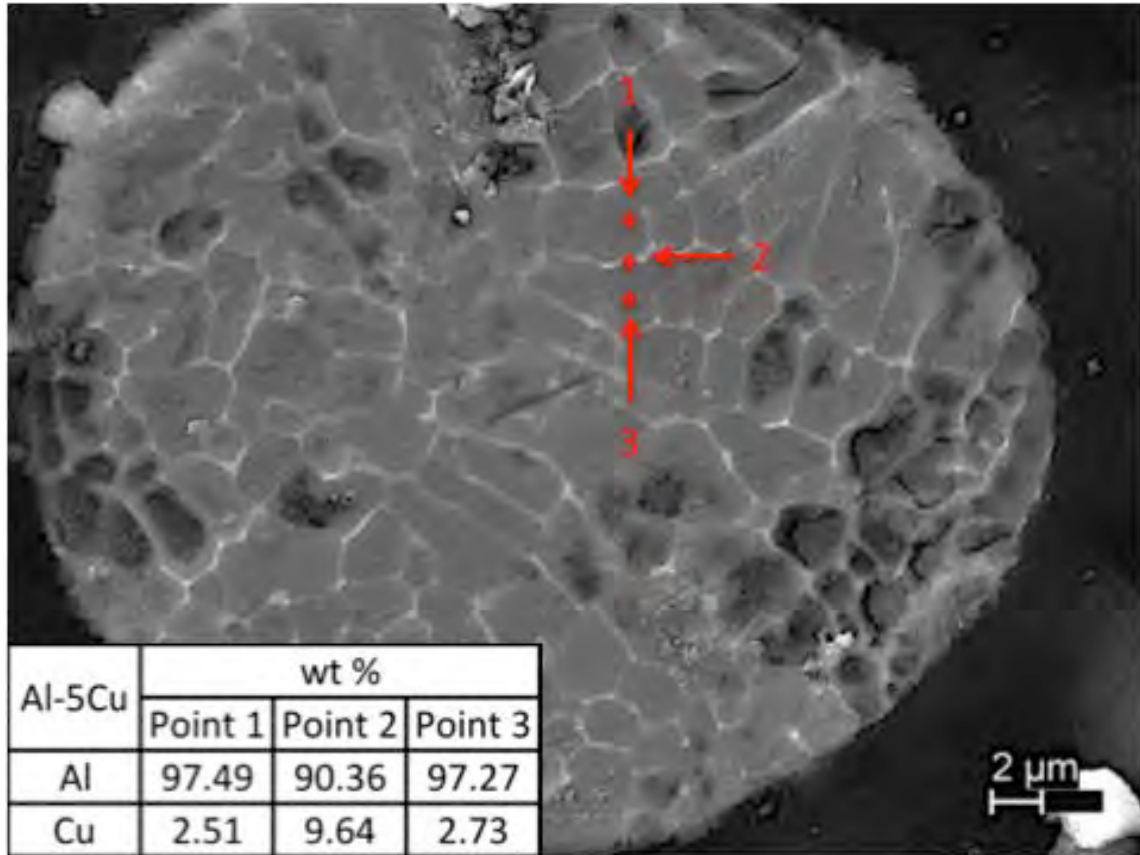


Figure 18. EDS quantification of Al-5Cu powder.

Table 6. Wt% Al and Cu from EDS $K\alpha$ measurements for Al-5Cu powder.

| Point 1 | | Point 2 | | Point 3 | |
|---------|------|---------|------|---------|------|
| Al | Cu | Al | Cu | Al | Cu |
| 95.42 | 4.58 | 92.05 | 7.95 | 95.14 | 4.86 |
| 97.29 | 2.71 | 92.58 | 7.42 | 96.77 | 3.23 |
| 96.54 | 3.46 | 93.02 | 6.98 | 96.13 | 3.87 |
| 97.49 | 2.51 | 90.36 | 9.64 | 97.27 | 2.73 |
| 97.29 | 2.71 | 93.21 | 6.79 | 96.77 | 3.23 |

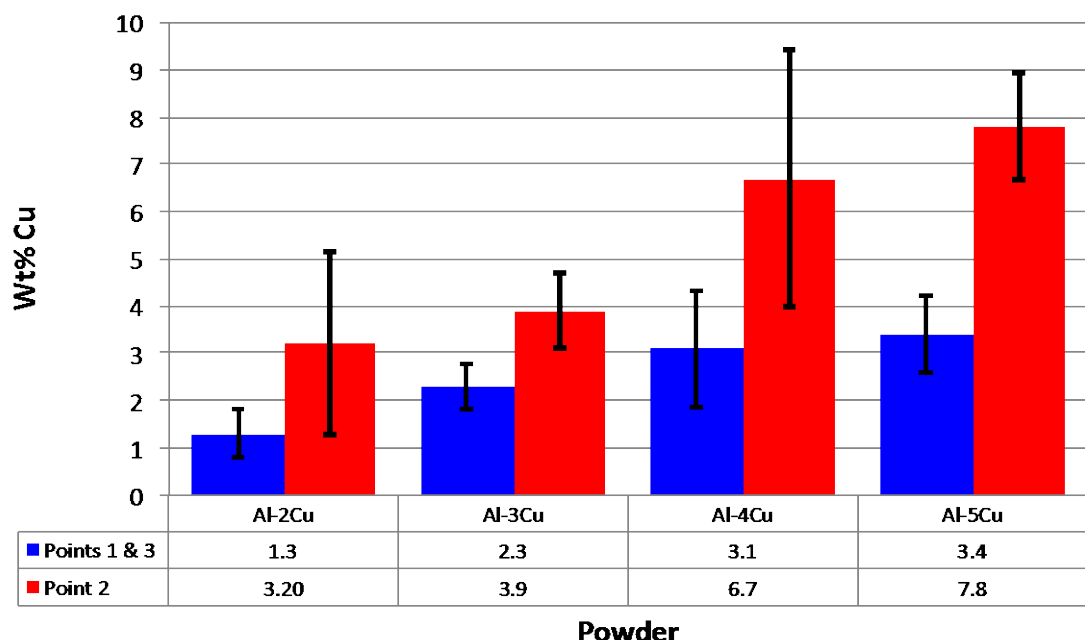


Figure 19. Average EDS values for the powders. Points 1 and 3 correspond to the center of cells while point 2 is the Cu rich boundary.

4. X-ray Maps

The EDX maps (Figures 20–23) provide a good visual display of the distribution of the copper and aluminum within a particle for each of the powders. Areas of concentrated copper are present at the cell boundaries while the entire cell has aluminum distributed throughout. As mentioned earlier, the darker regions of the particles where there are minimal amounts of copper or aluminum signal represent areas where selective etching of material took place during metallographic preparation.

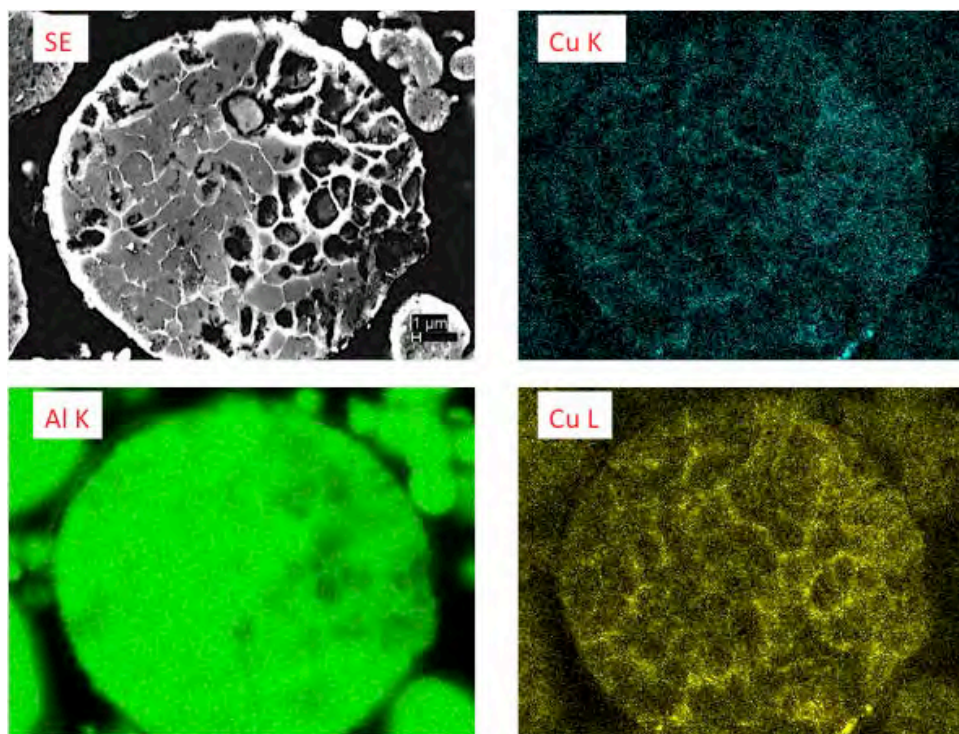


Figure 20. EDX maps showing the components (Al and Cu) of Al-2Cu.

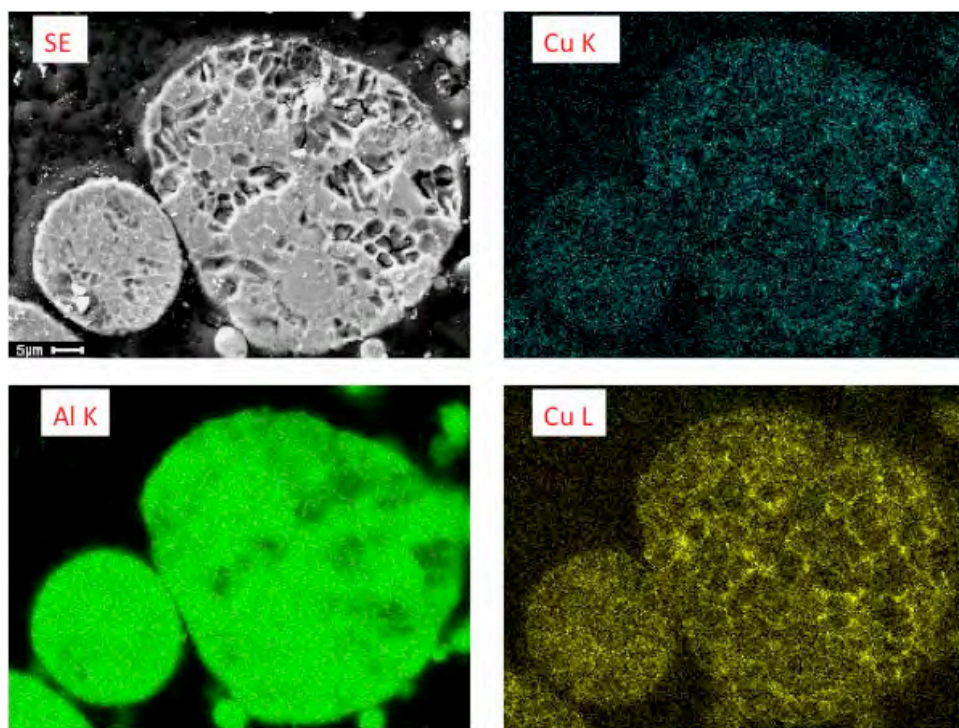


Figure 21. EDX maps showing the components (Al and Cu) of Al-3Cu.

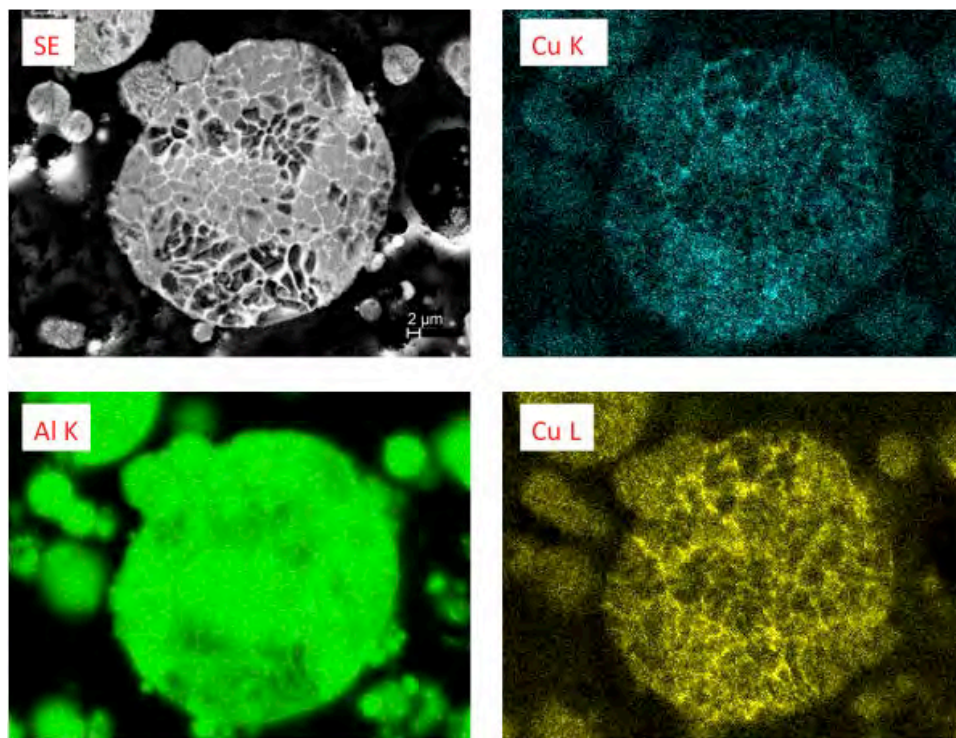


Figure 22. EDX maps showing the components (Al and Cu) of Al-4Cu.

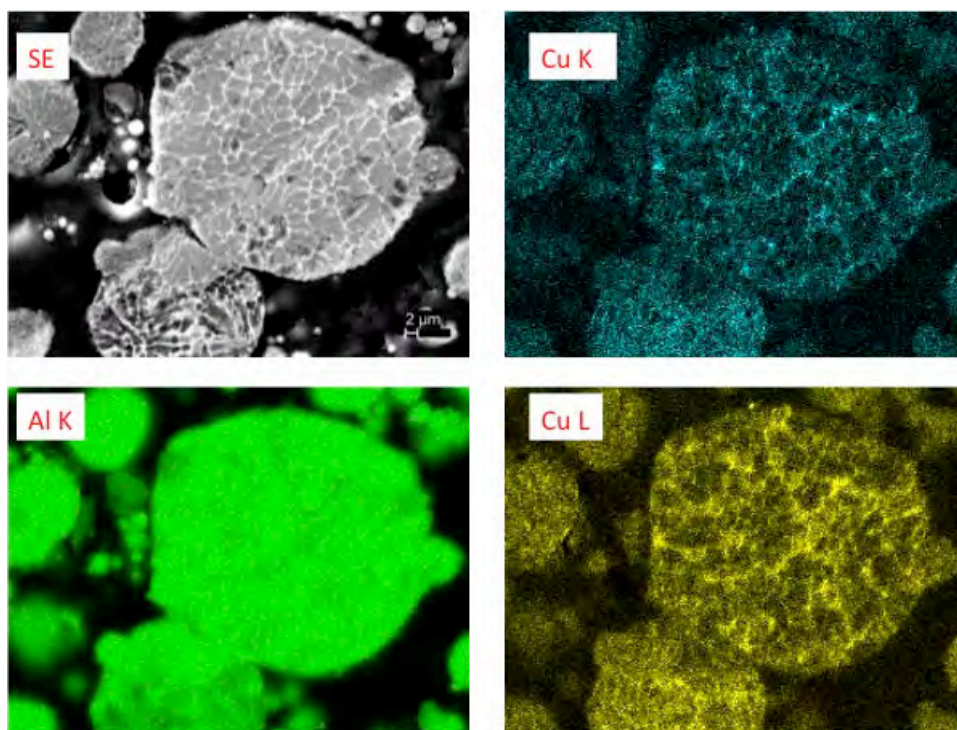


Figure 23. EDX maps showing the components (Al and Cu) of Al-5Cu.

5. X-ray Diffraction

The x-ray diffraction indicated that all of the powders have aluminum (FCC) and Al_2Cu (tetragonal) phases in their as-received state and an example of the phase identification of Al-5Cu is shown in Figure 24. Solid solution aluminum, being the matrix phase, is abundant in all of the powders while the weight fraction and hence the intensity of the Al_2Cu peaks increases with copper content. Figure 25 shows XRD data from all the four as-received powders, demonstrating the increasing fraction (and thus peak intensity) of the Al_2Cu phase with increasing copper content and it can be seen that the peaks for Al_2Cu in Al-2Cu are extremely minimal due to the low copper content in the powder.

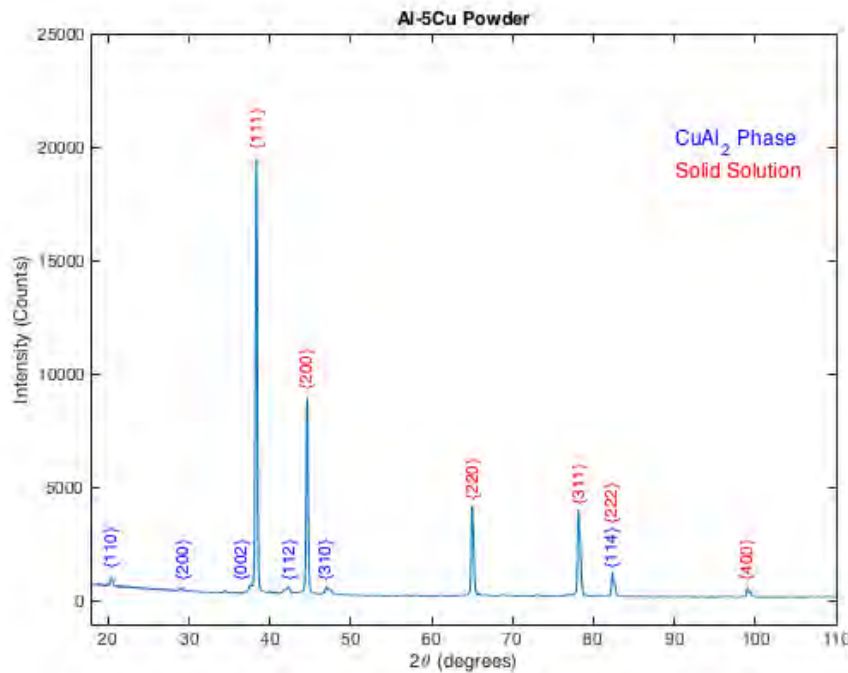


Figure 24. X-ray diffraction pattern for Al-5Cu powder as received.

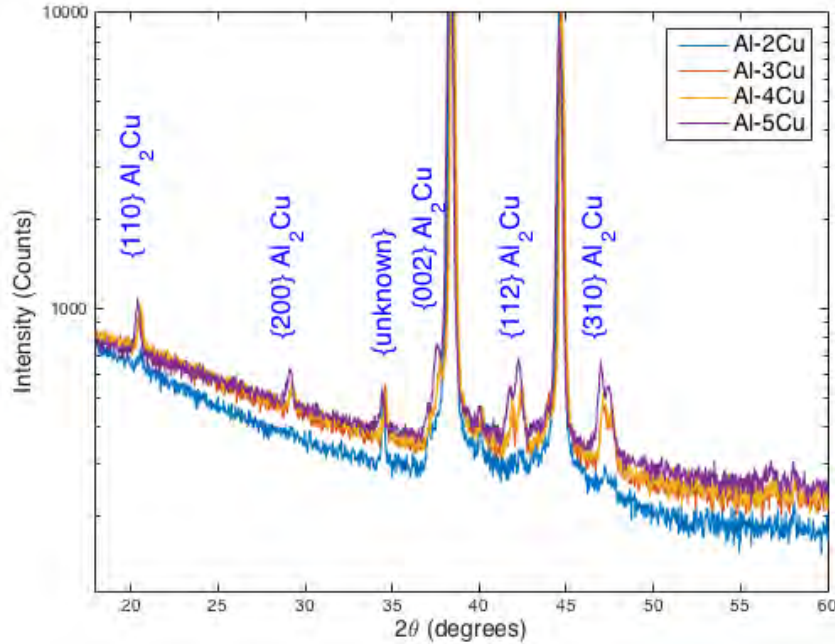


Figure 25. X-ray diffraction pattern of the four as-received powders. The unknown peak is a possible contaminant in the sample.

The powders were subjected to a heat treatment of 200°C for 11 hours to allow the powder microstructure to evolve toward equilibrium. The XRD patterns of the annealed powders show the FCC peaks belonging to aluminum and the tetragonal peaks of Al_2Cu . Figure 26 compares the XRD patterns from the as-received and annealed powders, illustrating the increase in the volume fraction of the Al_2Cu phase and the decrease in the lattice constant associated with the decreased supersaturation of the solid solution phase after annealing. The annealed powder XRD pattern displays an increase in Al_2Cu intensity compared to the as-received powder, which shows a shift toward equilibrium. The fractions of the Al_2Cu phase were calculated by the Rietveld analysis (plotted in Figure 27) performed on the XRD data from both the annealed and as-received powders; these were compared to the lever rule calculation at room temperature (21°C). As would be expected, the annealed powder consistently has a larger fraction of Al_2Cu phase than the as-received powder since the latter is produced under non-equilibrium solidification conditions. The fraction Al_2Cu for the annealed powder will approach but not exceed the prediction from the lever rule. The underestimate given by the Rietveld analysis may be from a lack of accuracy for this particular analysis, but the trends and the differences between the as-atomized and the annealed powder should be unaffected.

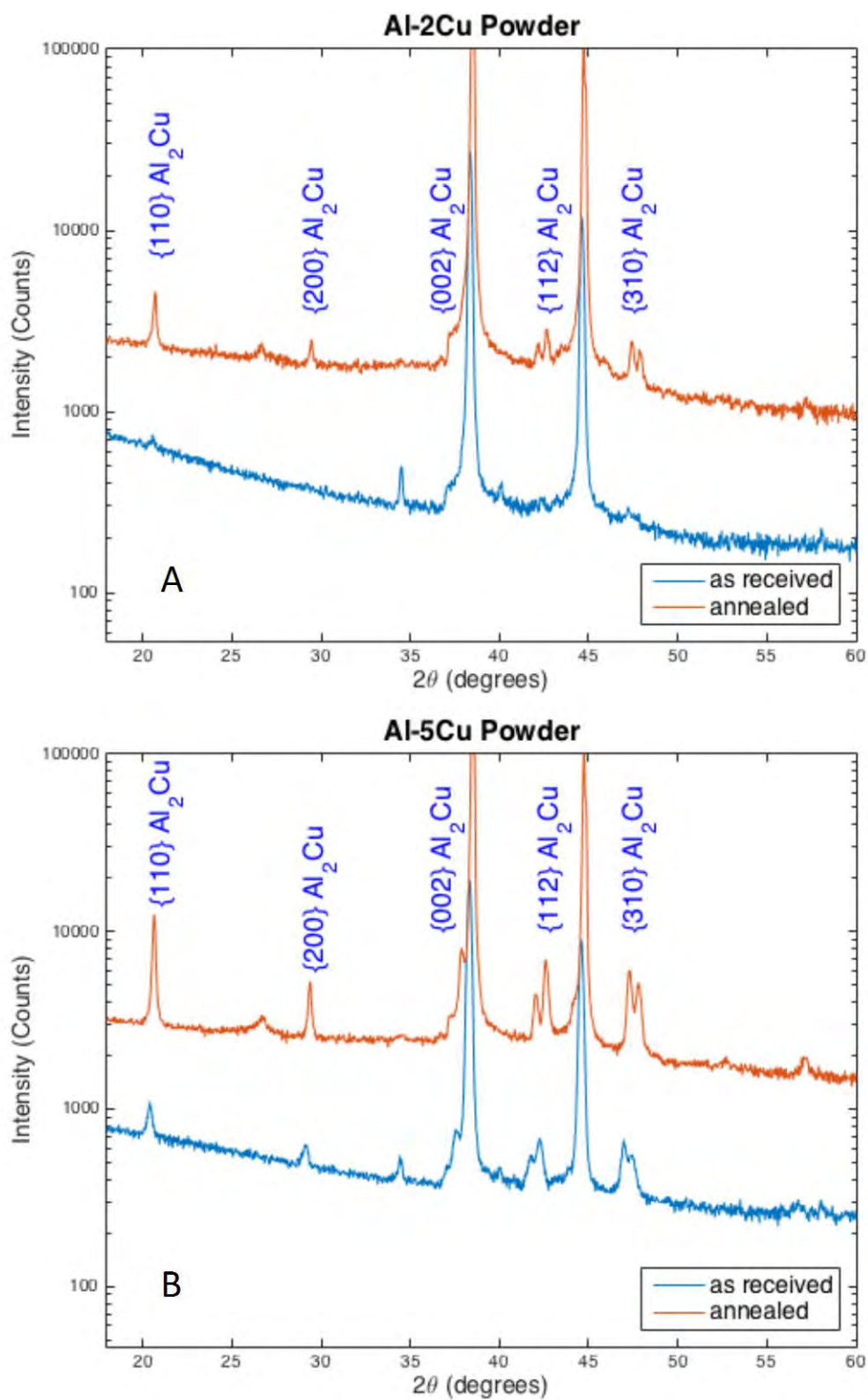


Figure 26. X-ray diffraction patterns comparing the as-received powders and the annealed powders for A) Al-2Cu and B) Al-5Cu, after [12].

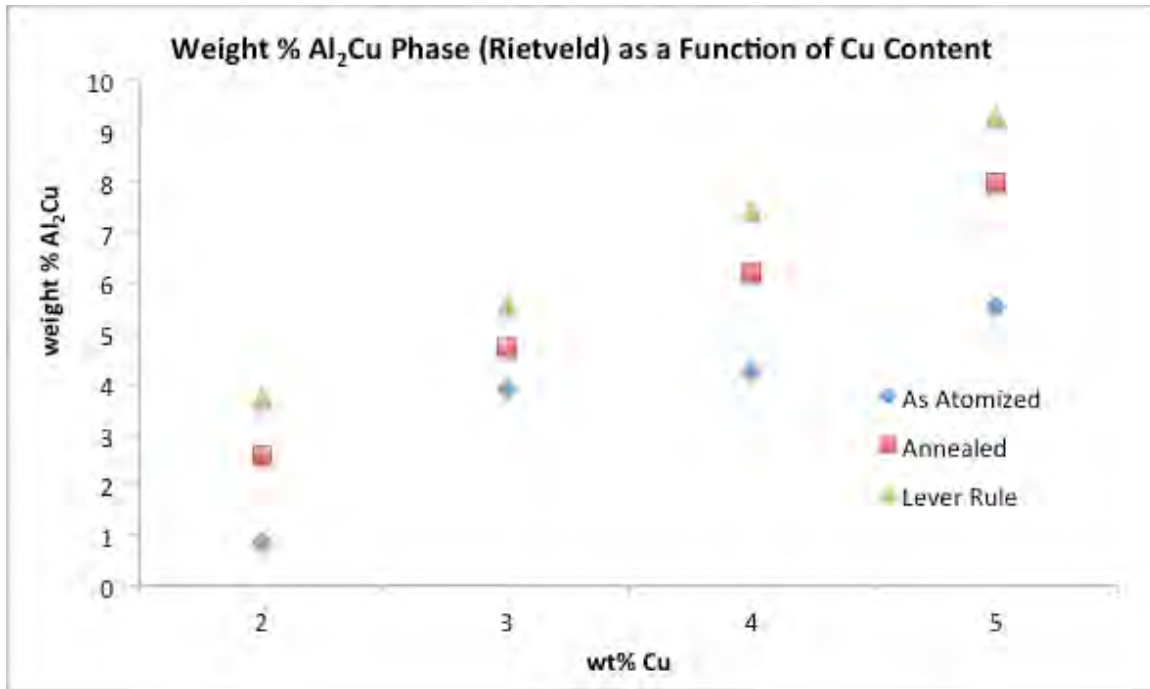


Figure 27. Wt% of Al₂Cu as determined by Rietveld analysis and the lever rule.

B. COLD SPRAY COATING CHARACTERISTICS

The cold spray coatings were characterized to determine how the Cu content, temperature, and pressure affect the dynamic mechanical properties of Al-Cu binary alloy powders during the cold spray process. The cold spray deposition was also studied to establish the how the microstructure and mechanical properties of the starting powder affect critical velocity.

1. Cold Spray Deposition Experiments

The deposition of Al-Cu powders was successful for all of the powders at various carrier gas (He) temperatures and pressures. Deposition experiments were performed according to Table 2, where the powders were sprayed in a 25 mm x 27 mm rectangular pattern that resulted in various thicknesses. The thickness and DE, a measure of how much of the powder adhered to the substrate, varied significantly for each experiment. Deposition thickness is a function of flow rate of the powder through the cold spray nozzle and the DE. All of the experiments were conducted using a single pass and the same *nominal* feed rate. All four powders were sprayed with the same carrier gas

temperature/pressure combination of 275°C/1.21 MPa (175 psi) with various results in thickness and DE (Figure 28). The thickness of the coatings in Figure 28 are 0.39 mm (0.0153 in), 0.92 mm (0.036 in), 0.13 mm (0.005 in), and 0.37 mm (0.0145 in) for the 2 wt %, 3 wt %, 4 wt %, and 5 wt % respectively. The copper content in the powders had no major effect on the DE. Reasonable DE's (>15%) were exhibited over a range of various carrier gas temperatures and pressures (Figure 29). High DE does not always result in a large deposition thickness since DE is dependent on the change in mass of the powder and substrate as seen in equation 4. The results of thickness and DE for the deposition experiments can be seen in Table 7.

Table 7. Summary of the spray conditions used for deposition experiments.

| Carrier Gas | He | He | He | He | He | He | He | He | He | He | He | He |
|-------------------------------|--------|--------|--------|--------|---------|---------|--------|--------|---------|---------|---------|---------|
| Powder | 2% | 2% | 2% | 2% | 2% | 3% | 4% | 5% | 5% | 5% | 5% | 5% |
| M _o (g) | 49.636 | 44.204 | 30.178 | 53.413 | 52.963 | 62.338 | 57.691 | 64.438 | 63.137 | 62.3550 | 59.2930 | 57.3170 |
| M _f (g) | 44.204 | 42.903 | 19.03 | 52.963 | 52.3640 | 59.6938 | 57.397 | 63.146 | 62.3550 | 59.2930 | 57.3170 | 56.1620 |
| Amount Sprayed (g) | 5.4321 | 1.3009 | 11.148 | 0.4499 | 0.5993 | 2.6437 | 0.2947 | 1.2925 | 0.7824 | 3.062 | 1.976 | 1.155 |
| Substrate | | | | | | | | | | | | |
| M _o (g) | 44.357 | 44.679 | 45.775 | 44.741 | 45.182 | 45.7970 | 43.88 | 45.129 | 45.453 | 44.2970 | 45.745 | 45.561 |
| M _f (g) | 45.754 | 45.422 | 48.585 | 44.826 | 45.434 | 46.799 | 44.028 | 45.668 | 45.688 | 45.012 | 46.183 | 46.163 |
| Pre-heat Temperature (°C) | 200 | 200 | 200 | 200 | 200 | 200 | 200 | 200 | 200 | 200 | 200 | 200 |
| Substrate thickness (inches) | 0.1291 | 0.1272 | 0.1272 | 0.1272 | 0.1272 | 0.1265 | 0.1260 | 0.1285 | 0.1264 | 0.1264 | 0.1272 | 0.1268 |
| Post spray thickness (inches) | 0.2423 | 0.1425 | 0.2287 | 0.1299 | 0.1346 | 0.1625 | 0.1310 | 0.1430 | 0.1350 | 0.1512 | 0.1386 | 0.1445 |
| Spray thickness (inches) | 0.1132 | 0.0153 | 0.1016 | 0.0027 | 0.0074 | 0.0360 | 0.0050 | 0.0145 | 0.0086 | 0.0248 | 0.0114 | 0.0177 |
| Substrate thickness (mm) | 3.28 | 3.23 | 3.23 | 3.23 | 3.23 | 3.21 | 3.20 | 3.26 | 3.21 | 3.21 | 3.23 | 3.22 |
| Post spray thickness (mm) | 6.155 | 3.62 | 5.81 | 3.30 | 3.42 | 4.13 | 3.33 | 3.63 | 3.43 | 3.84 | 3.52 | 3.67 |
| Spray thickness (mm) | 2.875 | 0.39 | 2.58 | 0.07 | 0.19 | 0.92 | 0.13 | 0.37 | 0.22 | 0.63 | 0.29 | 0.45 |
| Overlap (mm) | 1.2 | 1.2 | 1.2 | 1.2 | 1.2 | 1.2 | 1.2 | 1.2 | 1.2 | 1.2 | 1.2 | 1.2 |
| # Cycles | 10 | 10 | 10 | 10 | 10 | 10 | 10 | 10 | 10 | 10 | 10 | 10 |
| Passes | 1 | 1 | 1 | 1 | 1 | 1 | 1 | 1 | 1 | 1 | 1 | 1 |
| Pressure (psi) | 175 | 175 | 175 | 140 | 225 | 175 | 175 | 175 | 175 | 175 | 140 | 225 |
| Gun Temperature (°C) | 325 | 275 | 225 | 275 | 275 | 275 | 275 | 275 | 225 | 325 | 275 | 275 |
| Deposition Efficiency (%) | 25.71 | 57.08 | 25.21 | 18.89 | 42.03 | 37.91 | 50.22 | 41.70 | 30.05 | 23.35 | 22.19 | 52.16 |

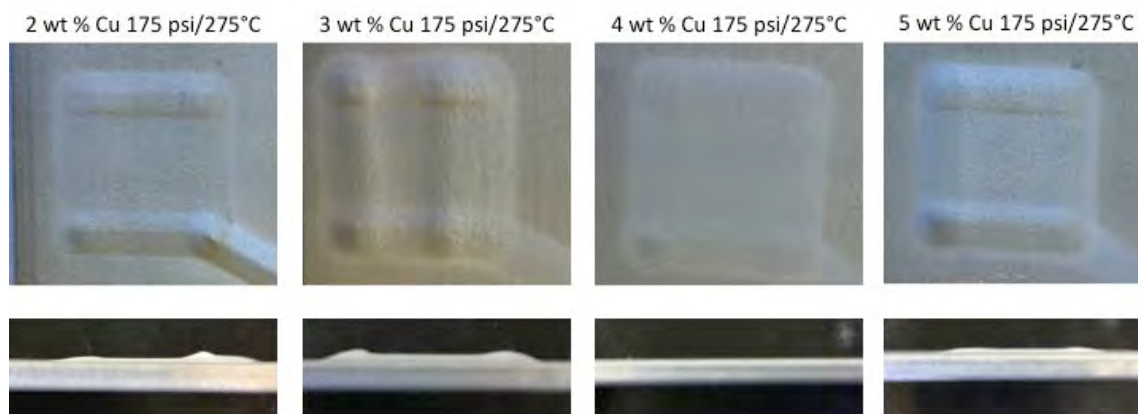


Figure 28. Deposition results for the carrier gas temperature of 275°C and pressure 1.21 MPa (175 psi).

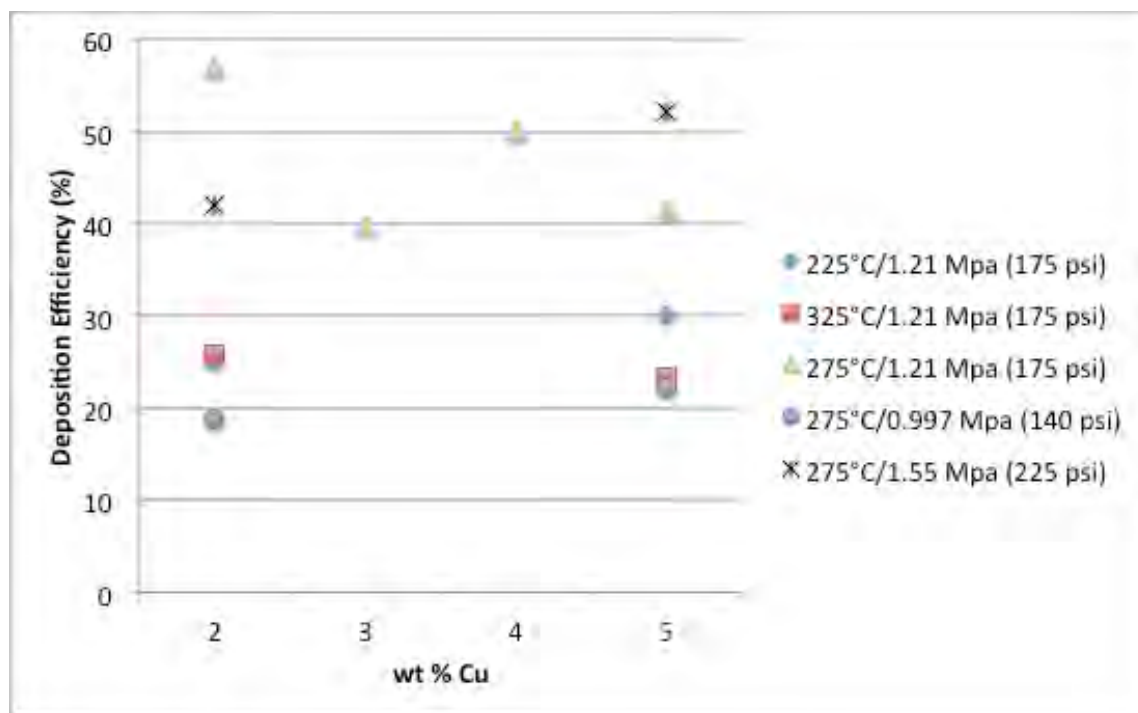


Figure 29. Deposition efficiency of the various temperature and pressure combinations for each of the powders.

Cold spray deposition experiments were also performed at NAVAIR in Patuxent River, Maryland using compressed air as the carrier gas. The experiments at NAVAIR used the same four Al-Cu powders and cold spray unit while the nozzle standoff distance

and carrier gas temperatures and pressures were different. Cold spray with compressed air is of great interest for portable repair applications. Due to the gas properties of compressed air, it was necessary to use higher carrier gas temperatures to achieve the critical velocity required for deposition. With the higher carrier gas temperatures, low pressure cold spray successfully deposited the Al-2Cu powder, albeit with relatively low deposition efficiencies (<5%). The compressed air experiments were unable to spray the higher copper content powders. A summary of the compressed air, low pressure cold spray deposition experiments can be seen in Table 8.

Table 8. Summary of cold spray parameters, thickness, and deposition efficiency for the cold spray experiments of Al-2Cu performed with compressed air.

| Pressure | | Temperature (°C) | Nozzle Stand-Off Distance (mm) | Thickness | | DE (%) |
|----------|-----|------------------|--------------------------------|-----------|--------|--------|
| Mpa | psi | | | in | mm | |
| 1.10 | 160 | 450 | 12 | 0.005 | 0.127 | 0.45 |
| 1.10 | 160 | 450 | 20 | 0.0015 | 0.0381 | 0.33 |
| 1.10 | 160 | 450 | 30 | 0 | 0 | 0.10 |
| 1.10 | 160 | 450 | 30 | 0 | 0 | 0.10 |
| 1.10 | 160 | 450 | 30 | 0 | 0 | 0.10 |
| 1.10 | 160 | 450 | 8 | 0.005 | 0.127 | 2.15 |
| 1.10 | 160 | 450 | 5 | 0.01 | 0.254 | 1.65 |
| 1.10 | 160 | 450 | 3 | 0.014 | 0.3556 | 2.77 |
| 1.21 | 175 | 450 | 12 | 0.015 | 0.381 | 1.62 |
| 1.21 | 175 | 450 | 16 | 0.005 | 0.127 | 1.84 |
| 1.21 | 175 | 450 | 20 | 0.008 | 0.2032 | 1.29 |
| 1.21 | 175 | 450 | 5 | 0.015 | 0.381 | 3.66 |
| 1.21 | 175 | 450 | 3 | 0.007 | 0.1778 | 4.66 |

2. Critical Velocity Experiments

Laser particle velocimetry was employed to investigate the effects of pressure, temperature, and copper content on critical velocity. The conditions in Table 3 and the associated deposition efficiencies were utilized to calculate the critical velocity for the Al-2Cu and Al-5Cu powders (Figure 30). All of the particle velocities present a Gaussian distribution with the average particle velocity between 570–640 m/s. The average particle velocity was calculated from the laser particle velocimetry and compared to the gas exit

velocity that was computed from MATLAB one-dimensional model. The summarized results in Table 9 suggest that lower copper content results in higher critical velocities.

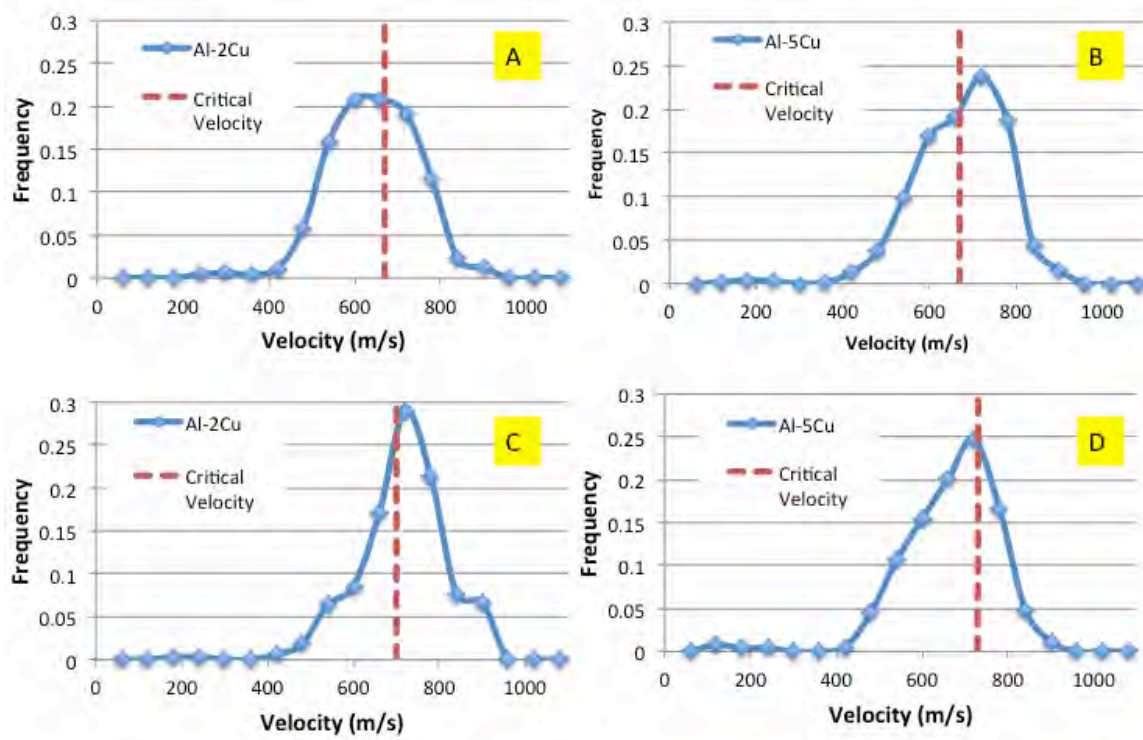


Figure 30. Measured particle velocities and calculated critical velocities for A) Al-2Cu at 225°C and 1.21 MPa (175 psi), B) Al-5Cu at 275°C and 1.21 MPa (175 psi), C) Al-2Cu at 275°C and 1.55 MPa (225 psi), and D) Al-5Cu at 325°C and 1.21 MPa (175 psi).

Table 9. Summary of critical velocity, deposition efficiency, calculated average particle velocity, and calculated average particle velocity.

| Parameters | | | 2% Cu | | | 5% Cu | | | Calculated Gas Exit Velocity (m/s) |
|-------------|----------|----------|-------------------------|-----------------------|--|-------------------------|-----------------------|--|------------------------------------|
| Temperature | Pressure | | Critical Velocity (m/s) | Deposition Efficiency | Calculated Average Particle Velocity (m/s) | Critical Velocity (m/s) | Deposition Efficiency | Calculated Average Particle Velocity (m/s) | |
| 275°C | 140 psi | 0.97 Mpa | 640 | 18.89% | 572 | 620 | 22.19% | 559 | 1994 |
| 225°C | 175 psi | 1.21 Mpa | 670 | 25.21% | 587 | 700 | 30.05% | 574 | 1901 |
| 275°C | 175 psi | 1.21 Mpa | 620 | 57.08% | 603 | 670 | 41.70% | 589 | 1994 |
| 325°C | 175 psi | 1.21 Mpa | 700 | 25.71% | 618 | 730 | 23.35% | 604 | 2083 |
| 275°C | 225 psi | 1.55 Mpa | 700 | 42.03% | 641 | 700 | 52.16% | 626 | 1994 |

The effects of carrier gas temperature and pressure on particle velocity can be understood by comparing the different particle velocities at the same temperature and pressure. Raising the temperature of the carrier gas has no measurable effect on particle velocity as seen in Figures 31A and 31B. The carrier gas pressure has a direct effect on particle velocity as an increase in carrier gas pressure results in a clear increase in particle velocity (Figures 31C and 31D). The effect of copper has no major effect on the particle velocity as the Al-2Cu and Al-5Cu have similar velocity profiles (Figure 32).

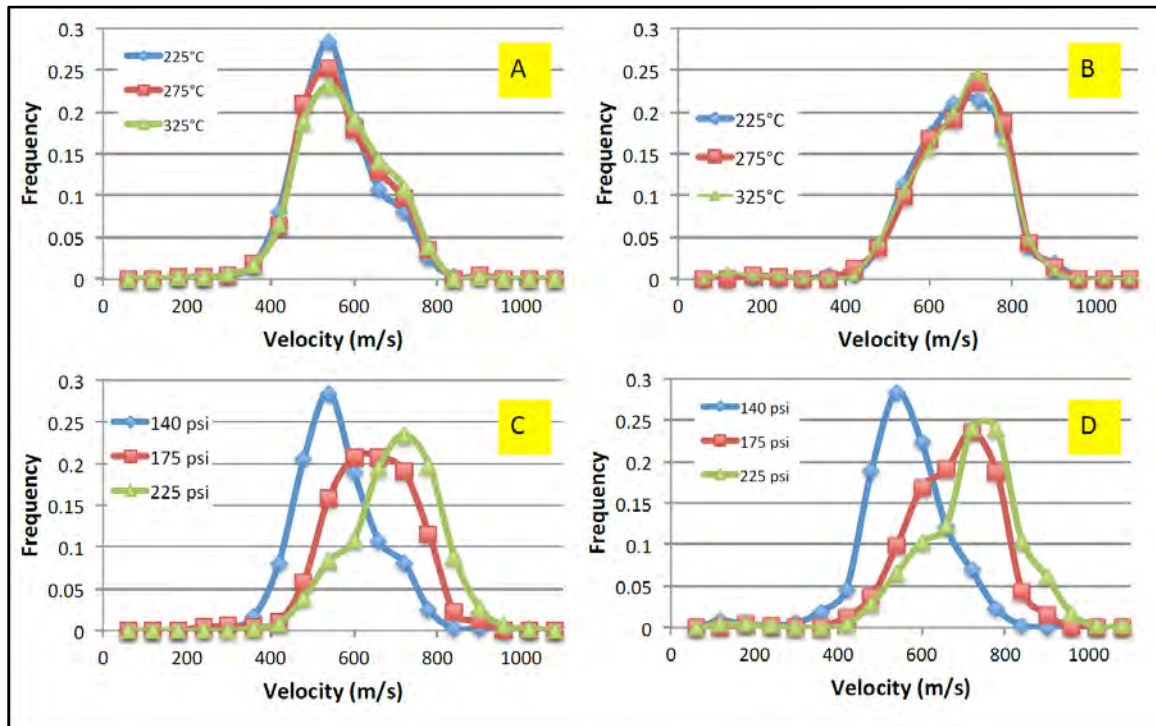


Figure 31. Measured particle velocity distributions of A) Al-2Cu at 0.97 MPa

(140 psi), B) Al-5Cu at 1.21 MPa (175 psi), C) Al-2Cu at 225°C, and D) Al-5Cu at 275°C.

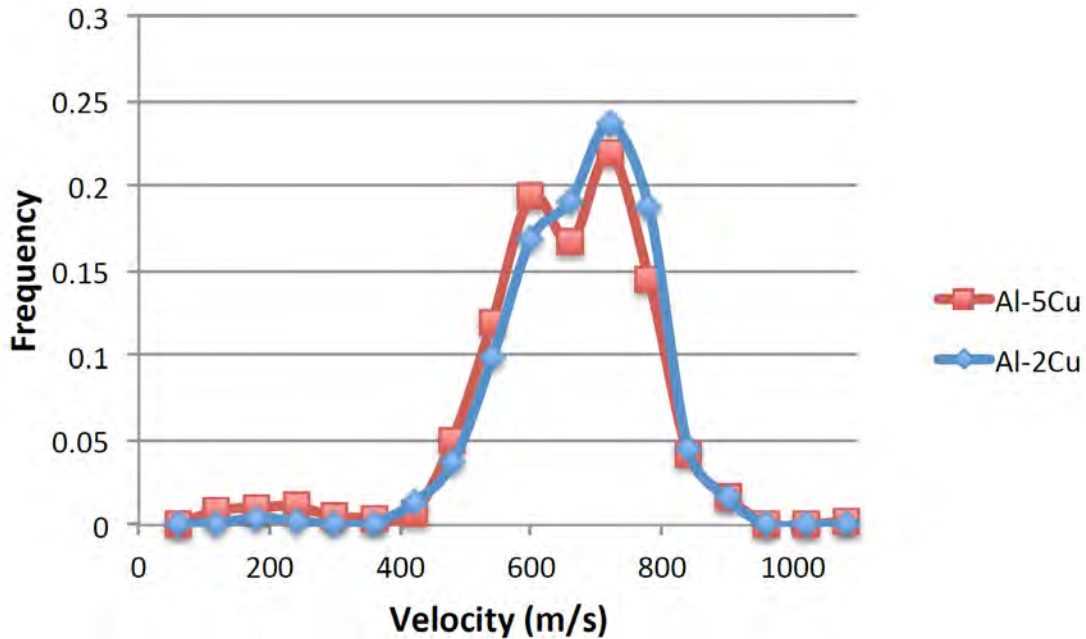


Figure 32. Velocity profile of Al-2Cu and Al-5Cu at 275°C and 1.21 MPa (175 psi).

3. MATLAB Simulation of Centerline SST UltiLife Nozzle

The cold spray parameters used in the deposition experiments were simulated in MATLAB to predict the particle exit velocities. When comparing the simulated and measured particle velocities, the mean velocity is relatively the same (Figure 33A and B). The simulated and measured velocities diverge as the velocity increases due to the limitations of the TECNAR CSM eVOLUTION and the particle sizes used in the simulation. The simulations used particle sizes obtained from the Horiba Laser Scattering Particle Size Analyzer, with some of them being smaller than 10 μm , outside of the lower limit of the laser velocimeter [32]. The carrier gas can accelerate smaller particles more easily, which is why the simulations predict higher velocities than the measured data. Another reason for the difference between simulated and measured velocities is the upper velocity limit of 1200 m/s for the laser velocimeter [32]. This does not allow particles

moving faster than 1200 m/s to be detected, another reason the smaller particles would not be measured. Accounting for the smaller particles, the frequency distribution in the simulated data is overall lower than the measured data. This resulted in the simulated data being plotted on a separate vertical axis to compare the shapes of the velocity profiles shown in Figure 33.

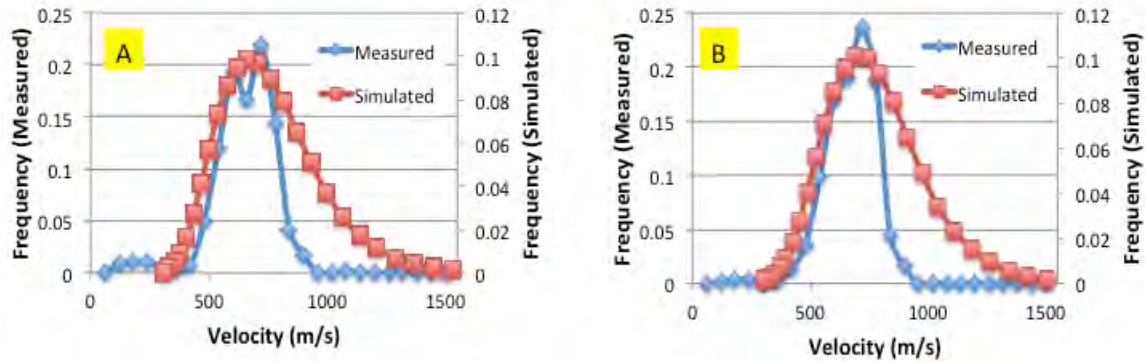


Figure 33. Comparison of measured and simulated particle velocities at 275°C and 1.21 MPa (175 psi) for A) Al-2Cu and B) Al-5Cu. Simulated data after [12].

Simulations were also run using the cold spray experiment parameters and Al-2Cu powder properties to investigate the effects of carrier gas temperature, pressure, and the position inside the nozzle versus particle velocity. The temperature versus particle velocity (Figure 4A) shows a linear increase in particle velocity as temperature increases. The velocities also increase as the pressure increases, which is consistent with the measured data. Figure 6A shows the effects of increasing temperature with regard to particle velocity. The particle velocity increases more than linearly and obtains a higher maximum velocity when the carrier gas temperature is increased than when pressure is increased. The heated carrier gas has more energy when it reaches the divergent part of the nozzle, which allows it to attain higher velocities and accelerate the particles to higher velocities [11]. The particle velocity with regard to position within the nozzle, as a function of carrier gas pressure and temperature, is shown in Figures 4B and 6B. Again it is shown that increasing the carrier gas pressure has a more significant effect on particle velocity than increasing carrier gas temperature. The simulation profiles support the

results obtained by laser particle velocimetry and the work of H. Assadi et al. [19]. Assadi et al. use a one-dimensional model to express the particle velocity at the end of the nozzle explicitly as a function of pressure, temperature, and particle size [19]. The one-dimensional model of [19] has two basic assumptions to velocity that prove true in the simulations performed, (1) the gas velocity at the exit is solely a function of temperature and (2) the particle velocity is a function of gas pressure.

4. Coating Microstructures

The cold spray experiments yielded dense coatings with slightly increased porosity at the coating/substrate interface. Since the cold spray process occurred at temperatures well below the solidus temperature of the alloy, the microstructure remains relatively unchanged in the coating from its powder form. The deposited coatings display a cellular structure similar to that found in the gas-atomized powder but heavily deformed (Figure 34–37). While the coatings in Figures 34–37 do appear dense, there is some micro-cracking between the sprayed particles as annotated in Figure 38 by the red arrows. This suggests that extreme deformation is causing the cracking or that the particles are not completely adhering to each other during the cold spray process. The Al-4Cu powder coating displayed higher amounts of cracking throughout the coating and at the coating/substrate interface (Figures 34–37). The cracks in the Al-4Cu coating appear to be primarily between the prior particles, indicating that the powder particles had poor adhesion during the cold spray experiment.

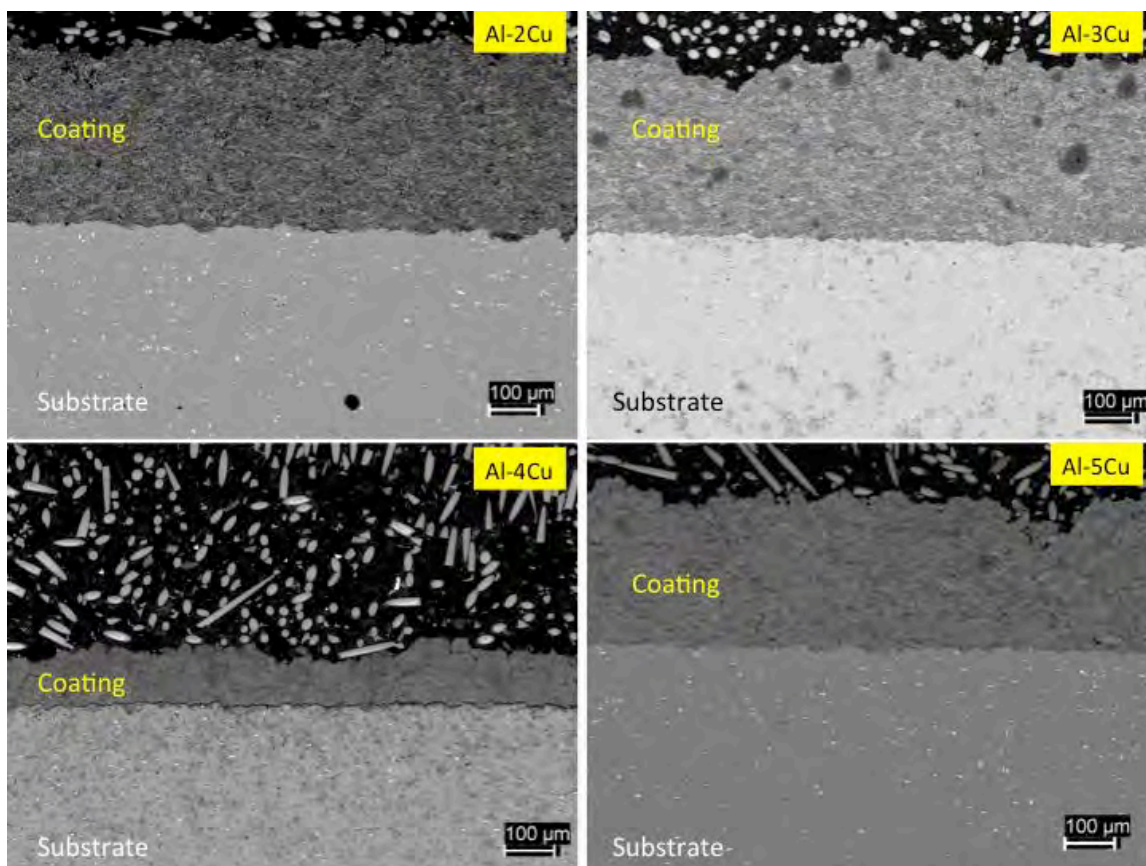


Figure 34. BSE micrographs, at 100x magnification, of cold-sprayed coating/substrate interface with helium gas at 275°C and 1.21 MPa (175 psi).

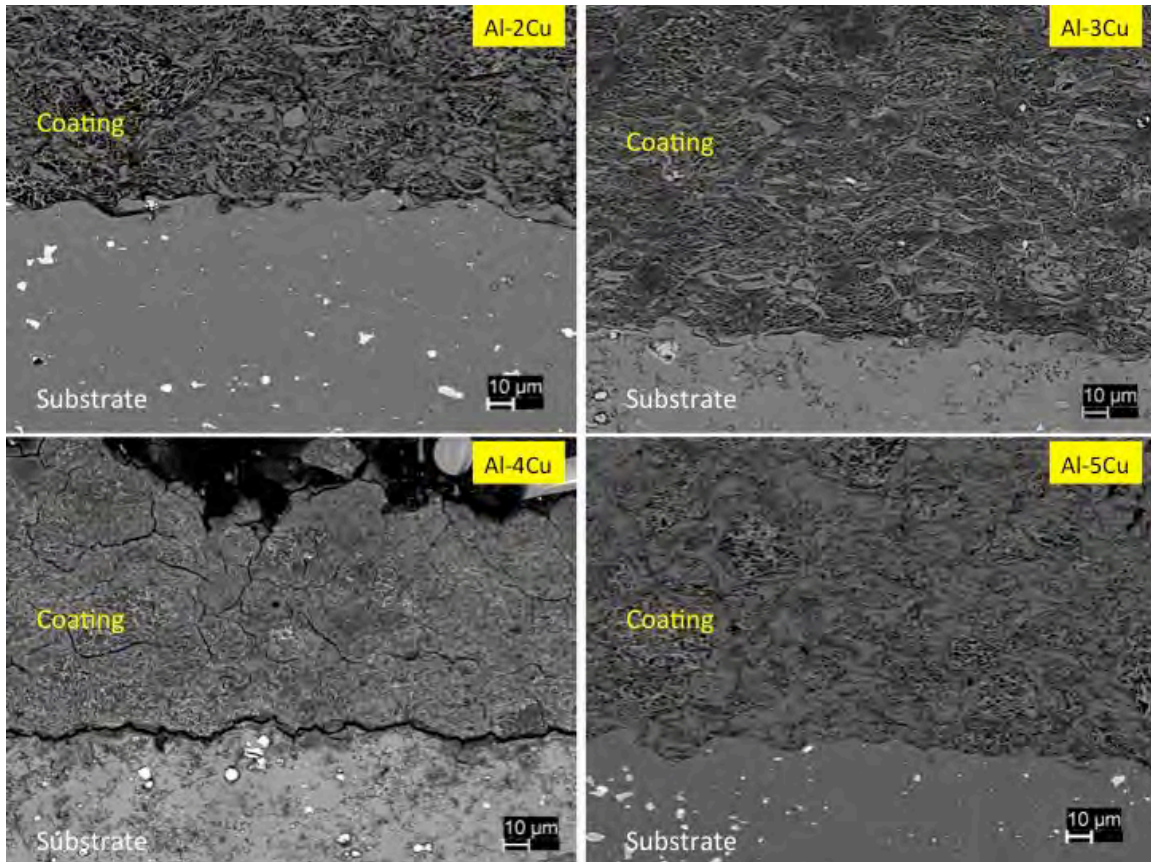


Figure 35. BSE micrographs, at 500x magnification, of cold-sprayed coating/substrate interface with helium gas at 275°C and 1.21 MPa (175 psi).

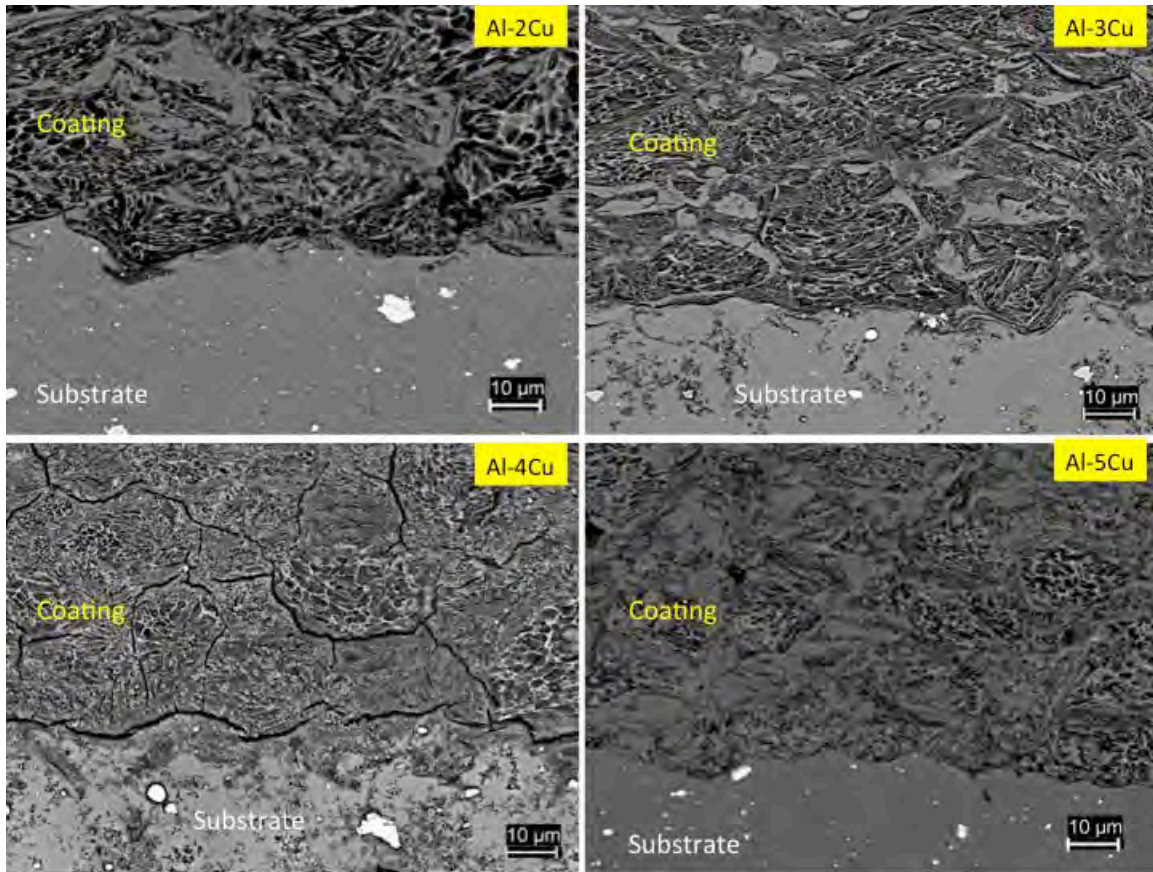


Figure 36. BSE micrographs, at 1000x magnification, of cold-sprayed coating/substrate interface with helium gas at 275°C and 1.21 MPa (175 psi).

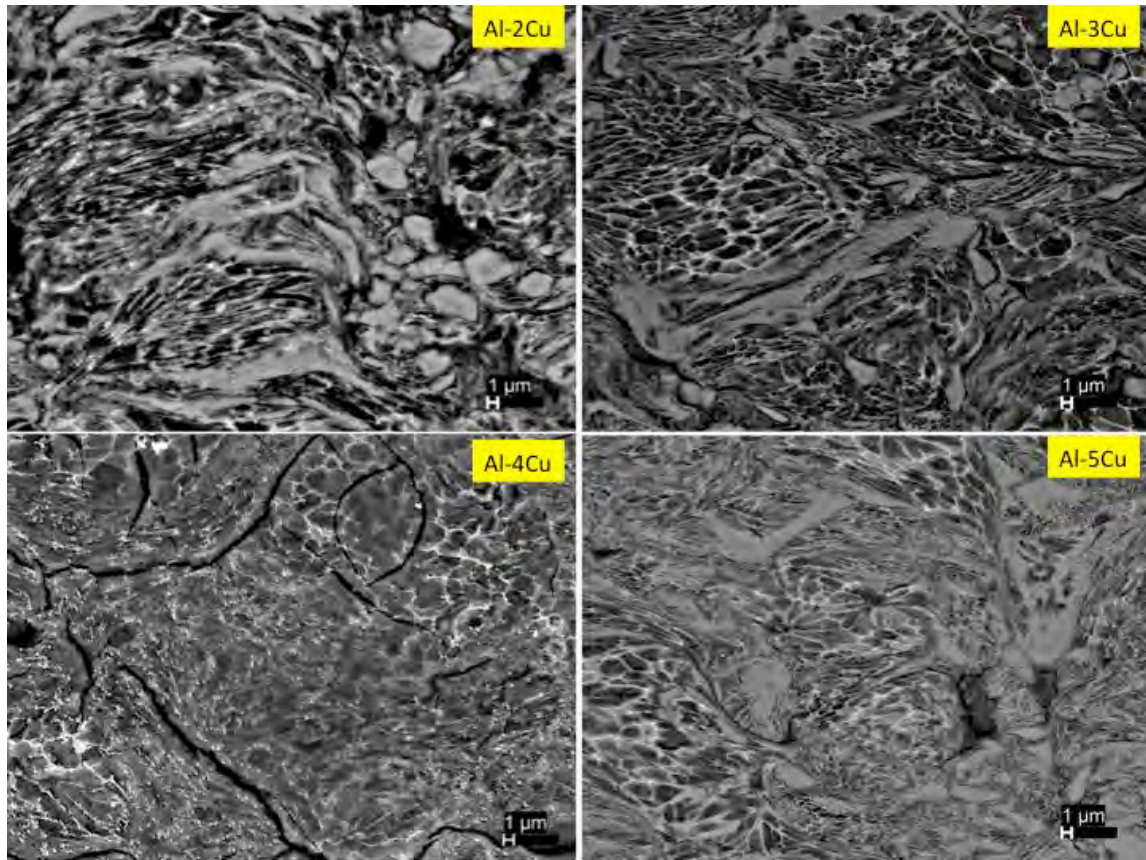


Figure 37. BSE micrographs, at 2000x magnification, of the center of the cold-sprayed coatings with helium gas at 275°C and 1.21 MPa (175 psi).

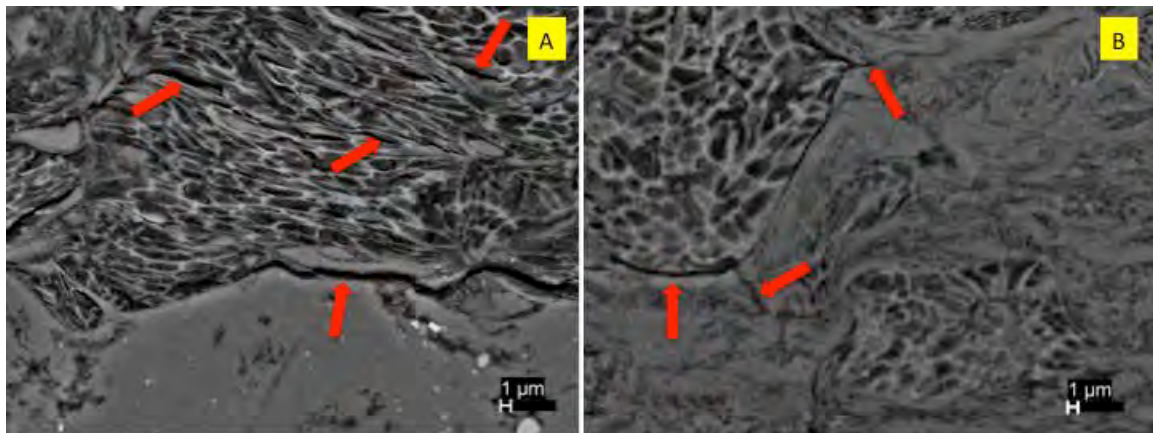


Figure 38. ILSE micrograph showing crack formation in cold spray deposition as depicted by the red arrows in A) Al-3Cu cold spray coating along the substrate interface and B) Al-5Cu cold spray coating.

5. Hardness

Vickers hardness measurements of the cold spray depositions show that the hardness increases as the copper content increases. Figure 39 shows that pressure and temperature affect the hardness of the coating. The Al-2Cu powder displays a significant range of hardness values for the different carrier gas pressure and temperature combinations (Figure 39). The Al-5Cu powder also shows a variety of hardness values, though not as varied as the Al-2Cu powder. At this time, the relationship between hardness and the carrier gas temperatures and pressures is not understood. Of note is the average hardness of the substrate, $134 \text{ Hv} \pm 8$, which is harder than all of the cold spray depositions. The average hardness values are $83 \text{ Hv} \pm 9$, $93 \text{ Hv} \pm 4$, $89 \text{ Hv} \pm 6$, and $102 \text{ Hv} \pm 4$ for the Al-2Cu, Al-3Cu, Al-4Cu, and Al-5Cu powders respectively. The highest measured hardness value was $107 \text{ Hv} \pm 4$ belonging the Al-5Cu sprayed at 1.55 MPa (225 psi) and 275°C (Table 10). It should be noted that the indentations in the coatings had cracks emanating from the indentations. As such, the Vickers hardness values may be lower than they would be for indentations without cracking.

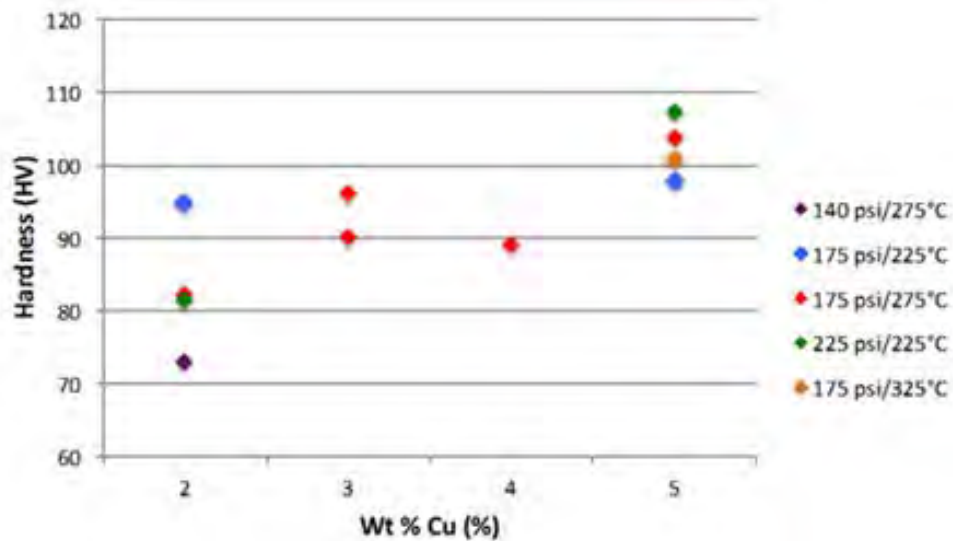


Figure 39. Hardness of the cold spray deposits as a function of wt% copper.

Table 10. Vickers hardness results of all four powders sprayed at various temperatures and pressures.

| Wt % Cu | Pressure | | Temperature (°C) | Average Hardness (HV) |
|---------|----------|-----|---------------------|-----------------------------|
| | Mpa | psi | | |
| 2 | 0.97 | 140 | 275 | 73 |
| 2 | 1.21 | 175 | 225 | 95 |
| 2 | 1.21 | 175 | 275 | 82 |
| 2 | 1.55 | 225 | 275 | 81 |
| 3 | 1.21 | 175 | 275 | 96 |
| 3 | 1.21 | 175 | 275 | 90 |
| 4 | 1.21 | 175 | 275 | 89 |
| 5 | 1.21 | 175 | 275 | 104 |
| 5 | 1.21 | 175 | 225 | 98 |
| 5 | 1.21 | 175 | 325 | 101 |
| 5 | 1.55 | 225 | 275 | 107 |

THIS PAGE INTENTIONALLY LEFT BLANK

IV. DISCUSSION

A. THE ROLE OF COPPER

One of the major focuses of this research is to study the effects of a systematic increase of the alloying agent in the feedstock powder used during the cold spray process. The copper content of each of the powders was evaluated for its effect on powder microstructure, cold spray deposition process, and the deposition coating properties.

The microstructures of the powders show cellular solidification as a result of gas atomization (Figure 14) [31]. The copper content in the powders has an inverse effect on cellular spacing. The number of cells formed from cellular solidification increase as copper content increases, thereby reducing the cellular spacing for a given range of particle cross sections as suggested by the data in Figure 15. The copper content directly affects the amount of copper at the copper rich cellular boundaries and the volume fraction of Al_2Cu in the powders. The EDS measurements show that the amount of copper, at the copper rich boundaries and in the center of the cells, is higher for the powders that have a higher bulk copper content. The Rietveld refinement (Figure 27) and lever rule calculations show that a larger volume fraction of Al_2Cu should be and is present in the powders with higher wt% copper.

The solidification cell size for the Al-Cu alloys studied here agrees well with the literature on gas atomization of aluminum alloys. It is well known that the cooling rate during solidification affects the cell or dendrite size in the solid; the faster the cooling rate, the smaller the cell size [35]. The connection between cooling rate and cell size for binary Al-Cu alloys has been examined Mullis et al. for gas atomized powders. The secondary dendrite arm spacing of gas atomized Al-4Cu powders was measured and then used to calculate the cooling rates during solidification. The cooling rates varied based on the particle cross section, from 320 K/s for the 212 to 150 μm sieve fraction to 11,000 K/s for the $< 38 \mu\text{m}$ sieve fraction [36]. The sieve fraction for powders in this thesis would be in this last range. The mean cellular size for the $< 38 \mu\text{m}$ sieve fraction is

slightly greater than 2 μm which is within the range, $1.62 \pm 0.51 \mu\text{m}$, of the Al-4Cu powder measurements performed for these thesis experiments.

The data suggests that the particle velocities are independent of the copper content in the feedstock powders. Table 9 shows that the Al-2Cu powder has a higher particle velocity than the Al-5Cu powder, a maximum difference of 15 m/s, which is approximately a 2% difference in velocity. The small variation in velocity is considered negligible and the measured particles velocities for Al-2Cu and Al-5Cu are believed to be similar. Figure 32 supports this, as the velocity profiles for Al-2Cu and Al-5Cu are approximately the same. From the experiments performed, no correlation can be made between copper content and DE or particle velocity and DE.

The hardness of the cold spray deposition coatings is directly affected by the copper content in the feedstock powder. The hardness value increases as the copper content is increased (Figure 39). There are multiple causes for the increase in hardness such as solid solution hardening, precipitation strengthening, and cold working as a result of cold spray. The aluminum-copper system benefits, in particular, from precipitation strengthening; although generally after a specific solutionizing-quench-aging sequence. The specific mechanism of hardening is not clear from the current data, but could be determined through further examination of the cold spray coatings in a transmission electron microscope. The increase in hardness is usually accompanied by a decrease in ductility, which was not measured during these experiments.

The cold spray deposition coatings display an overall uniform coating of deformed particles that is rather dense. The deposition coatings do display slight porosity along the substrate/coating interface and a minimal amount of lamellar cracking (Figure 38) at the particle/particle interfaces like that mentioned by J. Karthikeyan et al. during the spray of 1100 series aluminum [10]. Despite the deformation from the cold spray process, Figures 34–37 show that the initial cellular-solidification microstructures remain largely intact in the deposited coatings. The particles show a wide range of deformation with some close to their initial spherical shape while others are significantly flattened. L. Ajdelsztajn et al. theorized that particles with a greater degree of flattening should be softer and may have experienced lower cooling rates during gas atomization [37]. There

are two different deformation mechanisms present in the coating microstructure, one is total deformation of the particle and the other is a local deformation at prior particle boundaries [38]. The first mechanism of deformation results in a deformed cellular microstructure. The second mechanism generates very high shear strain levels at the prior particle boundaries. In all cases of deformation, the copper rich boundaries of the microstructure can be seen.

B. CALCULATION OF CRITICAL VELOCITY

The critical velocity is a theoretical value that particle velocity must exceed for deposition to occur. It has been proposed that critical velocity is a function of material properties of the powder and particle temperature [19], [39]. The density of the particles sprayed, a result of the copper composition, will affect the critical velocity of the powders. Assadi et al. states that particle density has an inverse relationship with critical velocity, meaning that as copper content increases, the critical velocity should decrease [19]. With the Al-5Cu powder denser than the Al-2Cu powder, the critical velocity calculations performed for the deposition experiments in this thesis do not support the mentioned density/critical velocity relationship (Table 9). The measured critical velocities either did not change or slightly increased for most of the experiments when copper content was increased. The critical velocities measured are comparable with those found from Equation 3, the critical velocity equation of Assadi et al. [19]. Equation 5 calculates critical velocity based on properties of the powder. The parameters used are for AA2024 and are shown with the resultant critical velocities are in Table 11.

$$v_{cr} = k_1 \sqrt{c_p (T_m - T_p) + 16 \frac{\sigma}{\rho_p} \left(\frac{T_m - T_p}{T_m - 293} \right)} \quad (5)$$

where

k_1 = dimensionless fitting parameter

c_p = specific heat capacity of the particle

T_m = average melting temperature

T_p = temperature of the particle

σ = tensile yield strength

ρ_p = particle density

Table 11. Parameters used to calculate critical velocity from equation 5.

| wt% Cu | c_p (J/g-°C) | T_m (°C) | T_p (°C) | σ (Mpa) | ρ_p (kg/m ³) | Critical Velocity (m/s) | |
|--------|-------------------|---------------|---------------|-------------------|----------------------------------|----------------------------|----------|
| | | | | | | k = 0.3 | k = 0.55 |
| 2 | 0.875 | 650 | 21 | 196 | 2825.2 | 475 | 871 |
| 3 | | | | 327 | 2887.8 | 580 | 1064 |
| 4 | | | | 392 | 2950.4 | 622 | 1140 |
| 4.5 | | | | 425 | 2981.7 | 641 | 1176 |

Accurately, estimating the critical velocity for the Al-Cu alloys is challenging. Following the approach of Assadi et al. [19], we see that the critical velocity of the particles should increase as a function of copper content (Figure 40). The major reason for this increase is the expected increase in flow stress, σ , as the copper content is increased. The addition of copper causes the tensile yield strength to increase more than particle density resulting in a higher critical velocity. At the present, the yield strength and UTS of these Al-Cu alloys particles is unknown. To estimate the values of yield strength in Figure 40, Vickers hardness values were utilized from the work of H. K. Hardy and T. J. Heal [40] for binary Al-Cu alloys. The Vickers hardness was converted to flow strength (MPa) using the Tabor approximation that the hardness is approximately 3 times the flow strength. It should also be noted that the values for Vickers hardness from Hardy's work were achieved after aging at 130°C for many hours, while the present powders are naturally aged for approximately one year. Nonetheless, the expected increase in strength for the powder particles as copper is added will cause a significant increase in the critical velocity.

The critical velocities predicted using the relationship from Assadi's work substantially overestimate the critical velocity compared to the measurements in this thesis. Assadi suggests a pre-factor, k, value of 0.5-0.6. Using k=0.55, the critical

velocities range from 871–1176 m/s, far too large for cold spray deposition of aluminum. The experimental values measured in this thesis were in the range of 620–730 m/s. A k -value of 0.3–0.35 produces critical velocities more in keeping with the experimentally measured range.

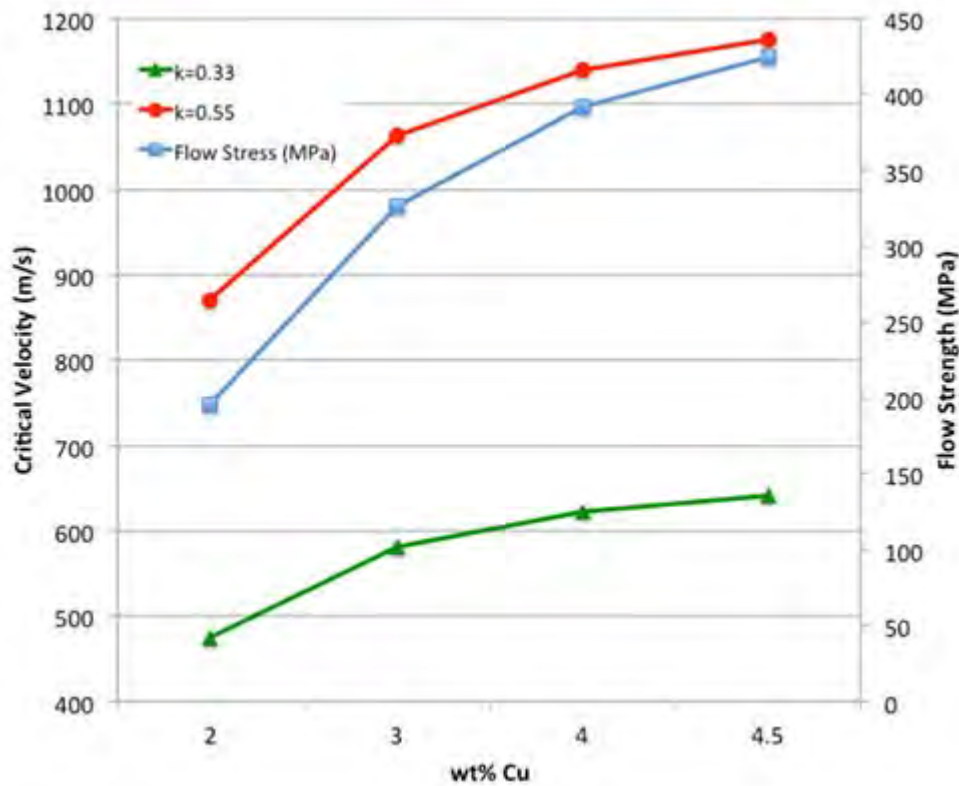


Figure 40. Critical velocity as determined by Equation 3 [19]. The Tabor approximation utilized the work of H. K. Hardy [40] to estimate the flow strength.

The effect of carrier gas temperature on critical velocity is inconclusive based on the results from the deposition experiments. The critical velocity decreased when carrier gas temperature went from 225°C to 275°C and then increased when temperature went from 275°C to 325°C for both the Al-2Cu and Al-5Cu powders. It should be noted that the measured velocity distributions for these depositions did not measurably change (Figure 31) as the temperature was increased, the only possible effect would be softening

of the particles; however, the thermal “soak time” may not be enough to make any significant difference.

The critical velocities of the powders sprayed are slightly higher than those in previous cold spray experiments for aluminum and aluminum alloys. The theoretical model of T. Schmidt et al. predicts the critical velocity prediction for aluminum, with a 25 μm diameter, sprayed onto aluminum to be from 620 m/s to 670 m/s [39]. V. Champagne states that for pure aluminum, an acceptable critical velocity for the deposition of pure aluminum is anything over 600 m/s [41]. E. Irissou et al. has reported critical velocity for Al_2O_3 and two aluminum powders to be 530 m/s, 660 m/s, and 580 m/s, respectively [42]. The Al-Cu powders sprayed for these experiments range between 620–730 m/s, which is higher than the other aluminum powders reported. The higher critical velocity range is reasonable and is a likely a result of the particles not being as soft as pure aluminum due to the addition of copper.

C. HOW FAR THE AS-RECEIVED POWDERS ARE FROM EQUILIBRIUM

During the gas atomization, the Al-Cu powders experienced rapid cooling to form the microstructures seen in Figure 14. The microstructures show cellular solidification that indicates that the powders did not achieve equilibrium during processing. Comparing XRD patterns of the as-received powders and heat-treated powders (Figure 26) shows the shift to a larger volume fraction of solid state Al_2Cu . The shift to a larger volume fraction of Al_2Cu as copper content increases can also be seen in the EDS measurements (Figure 19). Points 1 and 3 are measured in the center of the cell, comprised of mainly Al_2Cu . The Rietveld refinement (Figure 27) shows the difference between the as-received powders and the annealed powders and equilibrium as determined by the lever rule. As the copper content increases, the weight fraction of the Al_2Cu phase between the as-received powders and the annealed powders diverges. The increase in Al_2Cu phase due to an increase in copper content can also be seen in Figure 41. The Al-3Cu powder does show an exception to this (Table 12), as the difference between the as-received and annealed powders is the smallest for this copper content. The weight fraction of Al_2Cu from the lever rule appears to trend more closely to the annealed powder than the as-

received powder as copper content is increased. Though the annealed powder should be at equilibrium, the lever rule and annealed powder are not the same due to a lack of absolute accuracy in the Rietveld refinement. The inaccuracy in the Rietveld refinement does not affect the trends and the differences between the as-atomized powder and the annealed powder. While there is not enough data to accurately tell how far from equilibrium the powders are in their as-atomized condition, it is clear that the weight fraction of Al_2Cu increases both as the as copper content increases and after annealing.

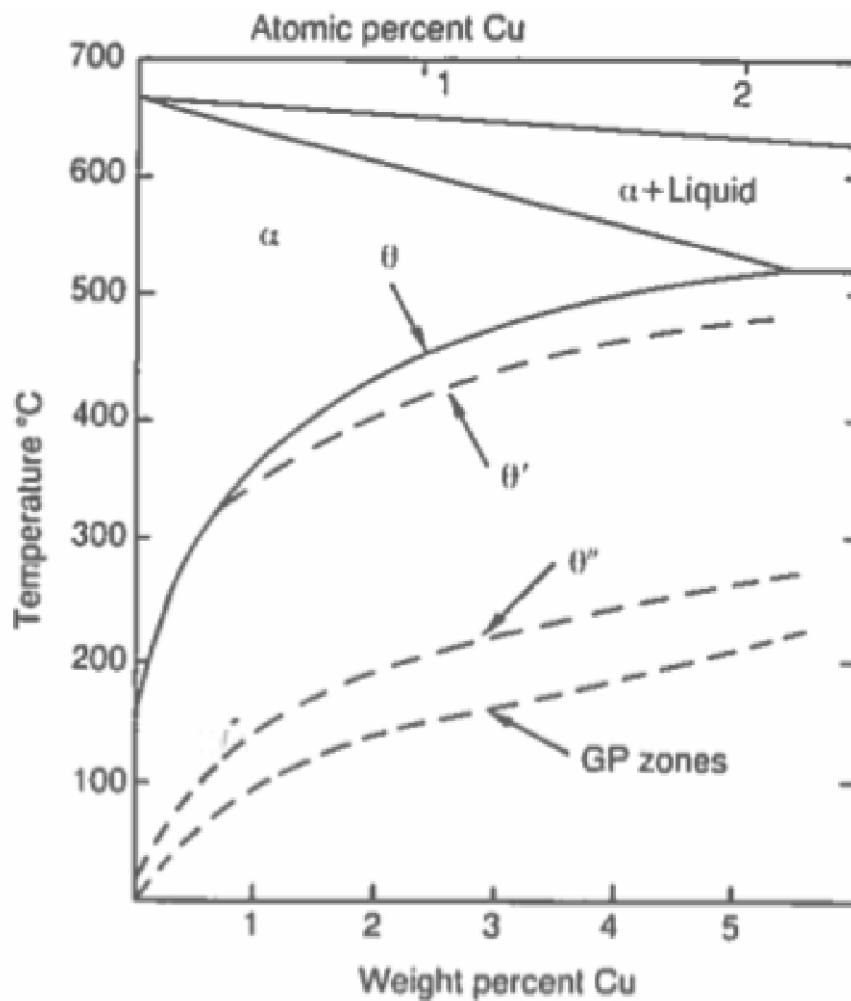


Figure 41. Binary phase diagram of the Al-Cu system showing the variation in solutionizing temperatures up to 6 wt% Cu, after [43].

Table 12. Weight percent of Al_2Cu as a result of x-ray diffraction for the as-received and annealed powders and from lever rule calculations.

| | Weight % Al_2Cu | | |
|--------------|---|-----------------|-------------------|
| wt%Cu | As Received | Annealed | Lever Rule |
| 2 | 0.87 | 2.58 | 3.72 |
| 3 | 3.92 | 4.74 | 5.59 |
| 4 | 4.25 | 6.19 | 7.45 |
| 5 | 5.55 | 7.99 | 9.31 |

D. RELATIONSHIP OF POWDER FLOWRATE, COATING THICKNESS, AND DEPOSITION EFFICIENCY

As a process used in material restoration, achieving a large thickness per spray pass is desired in cold spray. There is literature that suggests that thickness of the coating is a function of carrier gas temperature and feedstock powder flowrate [9], [44]. The results shown in Table 7 support the belief that thickness is a function of feedstock powder flow rate but they do not agree with carrier gas temperature affecting coating thickness. It is evident from Table 7 that regardless of the copper content, as more feedstock powder is sprayed the thickness increases.

With the Centerline (Windsor) SST Model Series C low-pressure cold spray system, the coating thickness is actually a function of the amount of feedstock powder loaded when the vibrational hopper is used. The vibrational hopper feed system was explained in a phone discussion with Centerline engineer Mark Delotta,

the hopper agitates the powder according to the feedrate setting. The amount of agitation is directly affected by the amount of powder in the hopper and increases as the amount of powder decreases. It should also be noted that the increase in feedrate is not linear with the vibrational hopper and the hopper is designed to be used with the manual spray gun and not the robot.

In all but four of the experiments conducted, the above feedrate explanation held true (Table 7). This leads to difficulty in controlling the feedrate and suggests the use of a powder feeder capable of providing a constant feedrate for the cold spray process when close control of thickness is desired.

Though a thick coating per pass is desirable, it is not an indicator of high DE. An increase in the amount of feedstock powder sprayed yields a larger thickness, which also allows for an increase in particle on particle interactions. The increased particle interactions can potentially prevent deposition causing less powder to adhere to the substrate or other deposited particles, which lowers DE. The results in Table 7 suggest that coating thickness and DE have an inverse relationship. This holds true for all of the experiments except for the Al-2Cu powder sprayed at 275°C and 0.97 MPa (140 psi).

THIS PAGE INTENTIONALLY LEFT BLANK

V. CONCLUSION

(1) Characterize Binary Al-Cu Alloy Powders

A series of Al-Cu binary alloy powders, with 2–5 wt% copper, were produced and characterized. While the size and shape of these powders was relatively uniform, the microstructure did systematically change, primarily through the increase in volume fraction of solid state Al_2Cu associated with the increase in bulk copper content. The copper content also affected cell boundary enrichment and cell sizes. The cell size itself was small, approximately 1.75 μm , and slightly decreased with increasing copper content.

(2) Produce Cold Spray Coatings using Al-Cu Alloy Powders

We successfully produced cold spray coatings for all four copper levels using helium as carrier gas. With compressed air, only the 2 wt% copper powder could be successfully sprayed. During the course of the deposition experiments, a one-dimensional model was used to accurately predict the particle velocities over various carrier gas pressures and temperatures. The measured critical velocity was between 620–700 m/s for Al-2Cu and did not vary significantly with increasing copper content. The relationship between powder feed rate and coating thickness was established and found to be independent of copper content.

(3) Investigate the basic microstructure-mechanical property relationships for cold spray deposited Al-Cu alloy coatings

High-density, well-bonded coatings were produced using helium as a carrier gas for all copper contents between 2–5 wt%. The cellular solidification microstructures that were present in the powders were largely intact with moderate deformation. The hardness of the coatings did increase with increasing copper content.

THIS PAGE INTENTIONALLY LEFT BLANK

APPENDIX. ONE-DIMENSIONAL MODEL SIMULATION MATLAB CODE

A. HELIUM

```

%%%%%%%%%%%%%%%%%%%%%%%%%%%%%%%%%%%%%%%%%%%%%%%%%%%%%%%%%%%%%%%%%%%%%%%%
%%%%%%%%%%%%%%%%%%%%%%%%%%%%%%%%%%%%%%%%%%%%%%%%%%%%%%%%%%%%%%%%%%%%%%%%
%
%           %
%   Centerline Nozzle One-Dimensional Model   %
%           %
%%%%%%%%%%%%%%%%%%%%%%%%%%%%%%%%%%%%%%%%%%%%%%%%%%%%%%%%%%%%%%%%%%%%%%%%
%%%%%%%%%%%%%%%%%%%%%%%%%%%%%%%%%%%%%%%%%%%%%%%%%%%%%%%%%%%%%%%%%%%%%%%%

% This model uses the area ratio of the nozzle to predict the gas
% pressure, temperature, and velocity along the nozzle up to the nozzle
% exit, utilizing the isentropic expansion equations.

% This model also predicts the particle velocity and particle temperature
% along the nozzle, up to the nozzle exit.

% Parameters that can be modified

% Gas Inlet Conditions
% P_go: inlet gas pressure [psi]
% T_go: inlet gas temperature [degC]
% U_gi: inlet gas velocity [m/sec]

% Gas Type Constants
% kappa: specific heat ratio for the gas
% R_h: specific gas constant

% Particle Properties
% Dp: the particle diameter [m]
% T_pi: initial temperature of particle [K]
% rho_p: density of particle [kg/m^3]
% Cp: specific heat of particle [J/kg-K]
% Up_i: initial particle velocity [m/sec]

% clear all
% close all
% clc

% Nozzle Characteristics

length = 126;
nozzle = linspace(0,126,126);
for j=1: length;

```

```

if j<=5
r(j,1)=-3.5/5*(j-1)+4.5;

```

```

elseif j>5
r(j,1)=2.15/120*(j)+0.8925;
end
end

NozzleArea = pi.*r.^2;

A_throat = NozzleArea(6);

aratio = NozzleArea./A_throat;

% Gas Inlet Properties

P_go = 225;      % [psi] inlet pressure
P_gi = P_go*6894.75729; % [Pa] inlet pressure
T_go = 275;      % [deg C] inlet temp
T_gi = T_go+273.15; % [K] inlet temp
U_gi = 40;       % [m/s] initial velocity

% Helium Properties
kappa = 1.66;    % specific heat ratio
R_h = 2.077;     % gas constant
rho_gi = P_gi/(1000*R_h*T_gi); % set initial gas density

% Particle Properties (Al-2Cu)
Dp = 116.21e-6; % diameter of particle [m]
T_pi = 300;     % initial temperature of particle [K]
rho_p = 2826;   % density of particle [kg/m^3], 3015 kg/m^3
               % for 5% Cu. 2826 kg/m^3 for 2% Cu.
Cp = 910;      % specific heat of particle [J/kg-K]
Cd = 0.47;
Up = 1;

% Outputs of Model (as a function of length along the nozzle)
% Pg: Gas Pressure [Pa]
% Tg: Gas Temperature [K]
% Ug: Gas Velocity [m/sec]
% rhog: Gas Density [kg/m^3]
% Up: Particle Velocity [m/sec]
% Tp: Particle Temperature [K]

% All other thermodynamic values can also be obtained but not are not
% outputted to the "createfigure" plot

% calculates constant in the gas velocity equation
Cnit= 2*(kappa/(kappa-1))*R_h*T_gi*1000;

```


% Manually Entered Values of the pressure ratio as a function of area ratio
 % as Solver couldn't solve the exponential function and find the roots

```
Pratio1=[.999358317; .998737359; .997145176; .992016005429711; 0.967559989427262;
0.488084943132466;
0.359127920170656; 0.310200003980210; 0.275259784181674; 0.247764607032805;
0.225107532475300; 0.205917151497742;
0.189360087557498; 0.174882435844313; 0.162092820026253; 0.150702167193243;
0.140489687746872; 0.131282274076478;
0.122941328310629; 0.115353964780749; 0.108426919914473; 0.102082208362417;
0.096253945448567; 0.0908859717935833;
0.085930043842133; 0.081344433061167; 0.077092825583738; 0.073143446813573;
0.069468357203175; 0.0660428797527548;
0.062845130644178; 0.059855630733058; 0.057056982177513; 0.054433596971072;
0.051971467672090; 0.0496579730284701;
0.047481711726954; 0.045432360106761; 0.043500549287789; 0.041677759083642;
0.039956225685067; 0.0383288611983731;
0.036789183342719; 0.035331253667411; 0.033949623142243; 0.032639284172274;
0.031395628156039; 0.0302144076238522;
0.029091702882145; 0.028023891856827; 0.027007623555420; 0.026039793957921;
0.025117524628255; 0.0242381433493700;
0.023399166717793; 0.022598284397934; 0.021833345058447; 0.021102343386980;
0.020403408484383; 0.0197347933359821;
0.019094865114476; 0.018482096538080; 0.017895057766986; 0.017332409200586;
0.016792894742944; 0.0162753357781050;
0.015778625608683; 0.015301724214751; 0.014843653661604; 0.014403493731683;
0.013980377929290; 0.0135734898791433;
0.013182059930296; 0.012805361960177; 0.012442710640023; 0.012093458630353;
0.011756994206475; 0.0114327389684121;
0.011120145739417; 0.0108186965716827; 0.0105279008844743; 0.0102472938960565;
0.00997643499960203; 0.00971490626976290;
0.00946231110004981; 0.00921827302606644; 0.00898243440768678; 0.00875445546019458;
0.00853401308891893; 0.00832080010210796;
0.00811452417147227; 0.00791490700643299; 0.00772168360610464; 0.00753460158970589;
0.00735342029841805; 0.00717791044925272;
0.00700785319751374; 0.00684303983721456; 0.00668327116123197; 0.00652835689970110;
0.00637811538002266; 0.00623237298461940;
0.00609096374543653; 0.00595372902022256; 0.00582051699311404; 0.00569118245731430;
0.00556558648031084; 0.00544359594917421;
0.00532508342963159; 0.00520992687834970; 0.00509800926392109; 0.00498921844651164;
0.00488344688009397; 0.00478059142854200;
0.00468055314990850; 0.00458323701855389; 0.00448855194056857; 0.00439641032292972;
0.00430672808437605; 0.00421942445714449;
0.00413442178584863; 0.00405164547409070; 0.00397102374922936; 0.00389248760537308;
0.00381597068494368; 0.00374140909760348];
```

% Solves for Pg, Tg, Ug, rho_g

for k=1:126;

Pg(k,1)=P_gi.*Pratio1(k,1);

```

Tg(k,1)=T_gi.*(Pratio1(k,1)^((kappa-1)/kappa));
Ug(k,1)=sqrt(Cnit*(1-Pratio1(k,1)^((kappa-1)/kappa))+U_gi^2);
rho_g(k,1)=rho_gi.*(Pratio1(k,1)^(1/kappa));

end

% Finding thermodynamic and hydrodynamic values utilizing linear
% interpolation based upon temperature of the gas
% Prandtl Number
% Dynamic Viscosity (www.nist.gov)
% Thermal Conductivity (www.nist.gov)

for k=1:126;
if Tg(k,1)<=800 && Tg(k,1)>=700
    Pr(k,1)=((Tg(k,1)-700)/(800-700))*(.654-.654)+.654;
    visc(k,1)=(1/1e7)*(((Tg(k,1)-700)/(800-700))*(394.2-358.6)+358.6);
    therm(k,1)=(1/1e3)*(((Tg(k,1)-700)/(800-700))*(307-292)+292);

elseif Tg(k,1)<=700 && Tg(k,1)>=600
    Pr(k,1)=((Tg(k,1)-500)/(700-500))*(.654-.668)+.668;
    visc(k,1)=(1/1e7)*(((Tg(k,1)-600)/(700-600))*(358.6-321.7)+321.7);
    therm(k,1)=(1/1e3)*(((Tg(k,1)-600)/(700-600))*(292-247)+247);

elseif Tg(k,1)<=600 && Tg(k,1)>=550
    Pr(k,1)=((Tg(k,1)-500)/(700-500))*(.654-.668)+.668;
    visc(k,1)=(1/1e7)*(((Tg(k,1)-550)/(600-550))*(321.7-302.7)+302.7);
    therm(k,1)=(1/1e3)*(((Tg(k,1)-550)/(600-550))*(247-229)+229);

elseif Tg(k,1)>=500 && Tg(k,1)<=550
    Pr(k,1)=((Tg(k,1)-500)/(700-500))*(.654-.668)+.668;
    visc(k,1)=(1/1e7)*(((Tg(k,1)-500)/(550-500))*(302.7-283.2)+283.2);
    therm(k,1)=(1/1e3)*(((Tg(k,1)-500)/(550-500))*(229-211.4)+211.4);

elseif Tg(k,1)>=450 && Tg(k,1)<=500
    Pr(k,1)=((Tg(k,1)-450)/(500-450))*(.668-.6715)+.6715;
    visc(k,1)=(1/1e7)*(((Tg(k,1)-450)/(500-450))*(283.2-263.15)+263.15);
    therm(k,1)=(1/1e3)*(((Tg(k,1)-450)/(500-450))*(211.4-194.7)+194.7);

elseif Tg(k,1)>=400 && Tg(k,1)<=450
    Pr(k,1)=((Tg(k,1)-400)/(450-400))*(.6715-.675)+.675;
    visc(k,1)=(1/1e7)*(((Tg(k,1)-400)/(450-400))*(260.7-242.7)+242.7);
    therm(k,1)=(1/1e3)*(((Tg(k,1)-400)/(450-400))*(194.7-179.5)+179.5);

elseif Tg(k,1)>=350 && Tg(k,1)<=400
    Pr(k,1)=((Tg(k,1)-350)/(400-350))*(.675-.6775)+.6775;
    visc(k,1)=(1/1e7)*(((Tg(k,1)-350)/(400-350))*(242.7-221.35)+221.35);
    therm(k,1)=(1/1e3)*(((Tg(k,1)-350)/(400-350))*(179.5-164.9)+164.9);

elseif Tg(k,1)>=300 && Tg(k,1)<=350
    Pr(k,1)=((Tg(k,1)-300)/(350-300))*(.6775-.680)+.680;
    visc(k,1)=(1/1e7)*(((Tg(k,1)-300)/(350-300))*(221.35-199.2)+199.2);

```

```

therm(k,1)=(1/1e3)*(((Tg(k,1)-300)/(350-300))*(164.9-149.9)+149.9);

elseif Tg(k,1)>=250 && Tg(k,1)<=300
    Pr(k,1)= ((Tg(k,1)-250)/(300-250))*(.680-.682)+.682;
    visc(k,1)=(1/1e7)*(((Tg(k,1)-250)/(300-250))*(199.2-176.0)+176.0);
    therm(k,1)=(1/1e3)*(((Tg(k,1)-250)/(300-250))*(149.9-133.8)+133.8);

elseif Tg(k,1)>=200 && Tg(k,1)<=250
    Pr(k,1)= ((Tg(k,1)-200)/(250-200))*(.682-.675)+.675;
    visc(k,1)=(1/1e7)*(((Tg(k,1)-200)/(250-200))*(176.0-151.4)+151.4);
    therm(k,1)=(1/1e3)*(((Tg(k,1)-200)/(250-200))*(133.8-115.1)+115.1);

elseif Tg(k,1)>=150 && Tg(k,1)<=200
    Pr(k,1)= ((Tg(k,1)-150)/(200-150))*(.675-.676)+.676;
    visc(k,1)=(1/1e7)*(((Tg(k,1)-150)/(200-150))*(151.4-124.9)+124.9);
    therm(k,1)=(1/1e3)*(((Tg(k,1)-150)/(200-150))*(115.1-95.0)+95.0);

elseif Tg(k,1)>=100 && Tg(k,1)<=150
    Pr(k,1)= ((Tg(k,1)-100)/(150-100))*(.676-.686)+.686;
    visc(k,1)=(1/1e7)*(((Tg(k,1)-100)/(150-100))*(124.9-95.29)+95.29);
    therm(k,1)=(1/1e3)*(((Tg(k,1)-100)/(150-100))*(95.0-73.0)+73.0);

elseif Tg(k,1)>=50 && Tg(k,1)<=100
    Pr(k,1)= ((Tg(k,1)-50)/(100-50))*(.686-.686)+.686;
    visc(k,1)=(1/1e7)*(((Tg(k,1)-50)/(100-50))*(95.29-60.66)+60.66);
    therm(k,1)=(1/1e3)*(((Tg(k,1)-50)/(100-50))*(73.0-46.23)+46.23);

elseif Tg(k,1)>=5 && Tg(k,1)<=50
    Pr(k,1)= ((Tg(k,1)-1)/(50-1))*(.759-.768)+.768;
    visc(k,1)=(1/1e7)*(((Tg(k,1)-1)/(50-1))*(60.66-12.24)+12.24);
    therm(k,1)=(1/1e3)*(((Tg(k,1)-1)/(50-1))*(46.23-2.69)+2.69);
end

end

% Solving for particle velocity

% Initializing all the vectors

Up=zeros(126,1);
Up(7,1)=1; % initialize the inlet velocity of powder
Cd=zeros(126,1);
Cd(7,1)=0.005; % initialize the drag coefficient
Re=zeros(126,1);

% Starts at point 7 (1 mm after nozzle throat)

for l=7:125

    % find acceleration, velocity, drag, and reynolds number
    % iterates to constantly solve for new reynolds and drag based upon
    % previous difference in particle and gas velocity

```

```

accel(l,1)=(3/4)*(Cd(l,1)*rho_g(l,1))/(Dp*rho_p)*(Ug(l,1)-Up(l,1))*(abs(Ug(l,1)-Up(l,1)));
Up(l+1,1)= Up(l,1)+accel(l,1)*.001/Up(l,1);
Up(l,1)= Up(l+1,1);
Re(l,1)= rho_g(l,1)*(Ug(l,1)-Up(l,1))*Dp/visc(l,1);
Cd(l+1,1)=(2.25*(Re(l,1)^(-0.31))+0.36*(Re(l,1)^0.06))^3.45;
Cd(l,1)=Cd(l+1,1);
Re(126,1)=rho_g(126)*Dp/visc(126)*(Ug(126)-Up(126));

end

% Solving for thermal properties of powder

Tp=zeros(126,1);
Tp(7,1)=300;

for k=1:126;
    Nu(k,1)=2+(0.6*(Re(k,1)^(1/2))*Pr(k,1)^(1/3));
    h(k,1)=Nu(k,1)*therm(k,1)/Dp;
end

for j=7:125;
    gradT(j,1)=(Tg(j,1)-Tp(j,1))*6*h(j,1)/(Cp*rho_p*Dp);
    Tp(j+1,1)=Tp(j,1)+gradT(j,1)*.001/Up(j,1);
    Tp(j,1)=Tp(j+1,1);
end

% Plotting the results

createfigure(nozzle, r, Pg, Ug, Up, Tg, Tp);

Max_Particle_Velocity = max(Up)

```

B. CREATFIGURE CODE

```
function createfigure(nozzle, r, Pg, Ug, Up, Tg, Tp)
% Plotting results
% Create figure
figure1 = figure;

% Create subplot
subplot1 = subplot(4,1,1,'Parent',figure1,'YTick',[0 5 10 15 20],...
    'XTickLabel',{' ',' ',' ',' ',' ',' '});
box(subplot1,'on');
grid(subplot1,'on');
hold(subplot1,'all');

% Create plot
plot(nozzle,r,'Parent',subplot1);

% Create ylabel
ylabel('Nozzle Contour, r(mm)');

% Create subplot
subplot2 = subplot(4,1,2,'Parent',figure1,...
    'YTickLabel',{'0','1','2','3','4'},...
    'YTick',[0 1000000 2000000 3000000 4000000],...
    'XTickLabel',{' ',' ',' ',' ',' ',' '});
box(subplot2,'on');
grid(subplot2,'on');
hold(subplot2,'all');

% Create plot
plot(nozzle,Pg,'Parent',subplot2);

% Create ylabel
ylabel('Pressure, P (MPa)');

% Create subplot
subplot3 = subplot(4,1,3,'Parent',figure1,'YTick',[0 200 400 600 800 1000],...
    'XTickLabel',{' ',' ',' ',' ',' ',' '});
box(subplot3,'on');
grid(subplot3,'on');
hold(subplot3,'all');

% Create plot
plot(nozzle,Ug, nozzle, Up,'Parent',subplot3);

% Create ylabel
ylabel('Velocity [m/s]');
legend('Ug','Up','Location','southeast')
% Create subplot
subplot4 = subplot(4,1,4,'Parent',figure1);
%% Uncomment the following line to preserve the X-limits of the axes
```

```

% xlim(subplot4,[0 300]);
%% Uncomment the following line to preserve the Y-limits of the axes
% ylim(subplot4,[0 650]);
box(subplot4,'on');
grid(subplot4,'on');
hold(subplot4,'all');

% Create plot
plot(nozzle,Tg, nozzle, Tp,'Parent',subplot4);

% Create ylabel
ylabel('Temperature [K]');
legend('Tg', 'Tp')
% Create xlabel
xlabel('Axial Distance, x (mm)');

```

LIST OF REFERENCES

- [1] T. Lang and E. Wingrove, “Cost of corrosion versus environmental severity,” LMI, Tech. Rep. AKN20T2, 2013.
- [2] J. Villafuerte and D. Wright, “Practical cold spray success: Repair of Al and Mg alloy aircraft components,” *Advanced Materials and Processes*, vol. 168, no. 5, pp. 53–55, May 2010.
- [3] V. K. Champagne and P. F. Leyman, “Cold Spray Process Development for the Reclamation of the Apache Helicopter Mast Support,” Army Research Laboratory, Aberdeen Proving Ground, MD, Tech. Rep. ARL-TR-4922, 2009.
- [4] B. DeForce et al., “Cold-Sprayed Aluminum Coatings for Magnesium Aircraft Components,” *Materials Performance*, vol. 48, no. 2, pp. 40–44, February 2009.
- [5] B.S. DeForce et al., “Cold Spray Al-5% Mg Coatings for the Corrosion Protection of Magnesium Alloys,” *Journal of Thermal Spray Technology*, vol. 20, no. 6, pp. 1352–1356, December 2011.
- [6] M. F. Smith, “Comparing cold spray with thermal spray coating technologies,” in *The Cold Spray Materials Deposition Process: Fundamentals and Applications*, V. K. Champagne, Ed. Boca Raton, FL: Woodhead, 2007, pp. 43–61.
- [7] R. Morgan et al., “Analysis of cold gas dynamically sprayed aluminium deposits,” *Materials Letters*, vol. 58, pp. 1317–1320, September 2004.
- [8] V.K. Champagne, “Introduction,” in *The Cold Spray Materials Deposition Process*, V.K. Champagne, Ed. Boca Raton, FL: Woodhead, 2007, pp. 1–7.
- [9] T. H. Van Steenkiste et al., “Kinetic Spray Coatings,” *Surface and Coatings Technology*, vol. 111, pp. 62–71, 1999.
- [10] J. Karthikeyan et al., “Microstructural and electrochemical characterization of cold-sprayed 1100 aluminum coating,” in *Proceedings of the International Thermal Spray Conference 10–12 May*, Osaka, Japan, 2004, pp. 341–346.
- [11] R. C. Dykhuizen and M. F. Smith, “Gas dynamic principles of cold spray,” *Journal of Thermal Spray Technology*, vol. 7, no. 2, pp. 205–212, June 1998.
- [12] J.F. Schiel, “The cold gas-dynamic spray and characterization of microcrystalline austenitic stainless steel,” M.S. thesis, MAE Dept., Naval Postgraduate School, Monterey, CA, 2014.

- [13] V. Champagne et al., "Theoretical and experimental particle velocity in cold spray," *Journal of Thermal Spray Technology*, vol. 20, no. 3, pp. 425–431, March 2011.
- [14] F. Gärtner et al., "The cold spray process and its potential for industrial applications," *Journal of Thermal Spray Technology*, vol. 15, no. 2, pp. 223–232, June 2006.
- [15] A. Papyrin, "The development of the cold spray process," in *The Cold Spray Materials Deposition Process: Fundamentals and Applications*, V.K. Champagne, Ed., Boca Raton, FL: Woodhead, 2007, pp. 26–31.
- [16] X.-J. Ning et al., "The effects of powder properties on in-flight particle velocity and deposition process during low pressure cold spray process," *Applied Surface Science*, vol. 253, pp. 7449–7455, March 2007.
- [17] D. L. Gilmore et al., "Particle velocity and deposition efficiency in the cold spray process," *Journal of Thermal Spray Technology*, vol. 8, no. 4, pp. 576–582, December 1999.
- [18] K. Sakaki, "The influence of nozzle design in the cold spray process," in *The Cold Spray Materials Deposition Process: Fundamentals and Applications*, V.K. Champagne, Ed., Boca Raton, FL: Woodhead, 2007, pp. 117–126.
- [19] H. Assadi et al., "On parameter selection in cold spraying," *Journal of Thermal Spray Technology*, vol. 20, no. 6, pp. 1161–1176, December 2011.
- [20] J. Pattison et al., "Standoff distance and bow shock phenomena in the Cold Spray process," *Surface & Coatings Technology*, vol. 202, pp. 1443–1454, 2008.
- [21] F. J. Brodmann, "Cold spray process parameters: Powder," in *The Cold Spray Materials Deposition Process: Fundamentals and Applications*, V. K. Champagne, Ed., Boca Raton, FL: Woodhead, 2007, pp. 108–113.
- [22] H. Koivuluoto et al., "High pressure cold sprayed (HPCS) and low pressure cold sprayed (LPCS) coatings prepared from OFHC Cu feedstock: Overview from powder characteristics to coating properties," *Journal of Thermal Spray Technology*, vol. 21, no. 5, pp. 1065–1075, September 2012.
- [23] B. Jodoin et al., "Effect of particle size, morphology, and hardness on cold gas dynamic sprayed aluminum alloy coatings," *Surface & Coatings Technology*, vol. 201, pp. 3422–3429, September 2006.
- [24] S. Celotto et al., "The economics of the cold spray process," in *The Cold Spray Materials Deposition Process: Fundamentals and Applications*, V.K. Champagne, Ed., Boca Raton, FL: Woodhead, 2007, pp. 72–101.

- [25] N. Matthews et al., “Application of supersonic particle deposition to enhance the structural integrity of aircraft structures,” *Science China Physic, Mechancis & Astronomy*, vol. 57, no. 1, pp. 12–18, January 2014.
- [26] R. Jones et al., “Supersonic particle deposition as a means for enhancing the structural integrity of aircraft structures,” *International Journal of Fatigue*, vol. 68, pp. 260–268, May 2014.
- [27] R. Ghelichi et al., “Microstructure and fatigue behavior of cold spray coated Al5052,” *Acta Materialia*, vol. 60, pp. 6555–6561, September 2012.
- [28] M.R. Rokni et al., “Microstructural stability of ultrafine grained cold sprayed 6061 aluminum alloy,” *Applied Surface Science*, vol. 290, pp. 482– 489, 2014.
- [29] D. A. Jones, *Principles and Prevention of Corrosion*, 2nd ed., Rose Kernan, Ed., Upper Saddle River, NJ: Prentice Hall, 1996.
- [30] L. Wang et al., “Formability and failure mechanisms of AA2024 under hot forming conditions,” *Materials Science and Engineering: A*, vol. 528, no. 6, pp. 2648–2656, March 2011.
- [31] L. Ajdelsztajn et al., “Cold-spray processing of a Nanocrystalline Al-Cu-Mg-Fe-Ni Alloy with Sc,” *Journal of Thermal Spray Technology*, vol. 15, no. 2, pp. 184–190, June 2006.
- [32] L. Pouliot, *CSM eVOLUTION Product Manual*. Canada: TECNAR Automation Ltd., 2013.
- [33] H. Koivuluoto and P. Vuoristo, “Effect of powder type and Composition on structure and mechanical properties of Cu + Al₂O₃ coatings prepared by using low-pressure cold spray process,” *Journal of Thermal Spray Technology*, vol. 19, no. 5, pp. 1081–1092, September 2010.
- [34] B. Zheng et al., “Gas Atomization of Amorphous Aluminum Powder: Part II. Experimental Investigation,” *Metallurgical and Materials Transcations B*, vol. 40B, pp. 995–1004, December 2009.
- [35] D. A. Porter, K. E. Easterling, and M. Y. Sherif, *Phase Transformations in Metals and Alloys*, 3rd ed., Boca Raton, FL, USA: CRC Press, 2009.
- [36] A.M. Mullis et al., “Estimation of cooling rates during close-coupled gas atomization using secondary dendrite arm spacing measurement,” *METALLURGICAL AND MATERIALS TRANSACTIONS B*, vol. 44B, pp. 992–999, August 2013.
- [37] L. Ajdelsztajn et al., “Cold gas dynamic spraying of a high temperature Al alloy,” *Surface & Coatings Technology*, vol. 201, pp. 2109–2116, July 2006.

- [38] B. Jodoin et al., "Effect of particle size, morphology, and hardness on cold gas dynamic sprayed aluminum alloy coatings," *Surface & Coatings Technology*, vol. 201, pp. 3422–3429, September 2006.
- [39] T. Schmidt et al., "Development of a generalized parameter window for cold spray deposition," *Acta Materialia*, vol. 206, pp. 729–742, February 2006.
- [40] H. K. Hardy and T. J. Heal, "Report on precipitation," *Progress in Metal Physics*, vol. 5, pp. 143–278, 1954.
- [41] V. Champagne et al., "Cold spray for repair of magnesium components," Army Research Laboratory, Final Report 2011.
- [42] E. Irissou et al., "Investigation of Al-Al₂O₃ cold spray coating formation and properties," *Journal of Thermal Spray Technology*, vol. 16, no. 5, pp. 661–668, December 2007.
- [43] G.W. Lorimer, "Precipitation in aluminum alloys," in *Precipitation Processes in Solids*, K.C. Russell and H.I. Aaronson, Ed. Warrendale, PA: Metallurgical Society of AIME, 1978, pp. 87–120.
- [44] E. Sansoucy et al., "Mechanical characteristics of Al-Co-Ce coatings produced by the cold spray process," *Journal of Thermal Spray Technology*, vol. 16, no. 5, pp. 651–660, December 2007.

INITIAL DISTRIBUTION LIST

1. Defense Technical Information Center
Ft. Belvoir, Virginia
2. Dudley Knox Library
Naval Postgraduate School
Monterey, California